UNIVERSITY OF ALBERTA

# Pump-Signal Combiners for Optical Amplifier Arrays Based on Multimode Interference

BY

**Naga Harini Gopaluni**

©

A thesis submitted to the Faculty of Graduate Studies and Research in partial fulfillment of the requirements for the degree of Master of Science

DEPARTMENT OF ELECTRICAL AND COMPUTER ENGINEERING

EDMONTON, ALBERTA, CANADA
FALL 2003

National Library
of Canada

Acquisitions and
Bibliographic Services

395 Wellington Street
Ottawa ON K1A 0N4
Canada

Bibliothèque nationale
du Canada

Acquisisitons et
services bibliographiques

395, rue Wellington
Ottawa ON K1A 0N4
Canada

*Your file Votre référence*
*ISBN: 0-612-87767-1*
*Our file Notre référence*
*ISBN: 0-612-87767-1*

The author has granted a non-exclusive licence allowing the National Library of Canada to reproduce, loan, distribute or sell copies of this thesis in microform, paper or electronic formats.

The author retains ownership of the copyright in this thesis. Neither the thesis nor substantial extracts from it may be printed or otherwise reproduced without the author's permission.

L'auteur a accordé une licence non exclusive permettant à la Bibliothèque nationale du Canada de reproduire, prêter, distribuer ou vendre des copies de cette thèse sous la forme de microfiche/film, de reproduction sur papier ou sur format électronique.

L'auteur conserve la propriété du droit d'auteur qui protège cette thèse. Ni la thèse ni des extraits substantiels de celle-ci ne doivent être imprimés ou aturement reproduits sans son autorisation.

Canada

UNIVERSITY OF ALBERTA

LIBRARY RELEASE FORM

NAME OF THE AUTHOR: **Naga Harini Gopaluni**

TITLE OF THESIS: **Pump-Signal combiners for optical amplifier arrays based on multimode interference**

DEGREE: **Master of Science**

YEAR THIS DEGREE GRANTED: **2003**

Permission is hereby granted to the University of Alberta Library to reproduce single copies of this thesis and to lend or sell such copies for private, scholarly or scientific research purposes only.

The author reserves all other publication and other rights in association with the copyright in the thesis, and except as herein before provided, neither the thesis nor any substantial portion thereof may be printed or otherwise reproduced in any material from whatever without the author's prior written permission.

Canada

Date: Sept 25, 2003

**UNIVERSITY OF ALBERTA**

FACULTY OF GRADUATE STUDIES AND RESEARCH

The Undersigned certify that they have read, and recommend to the Faculty of Graduate Studies and Research for acceptance, a thesis entitled **Pump - Signal Combiners for Optical Amplifier Arrays Based on Multimode Interference** submitted by Harini Gopaluni in partial fulfillment of the requirements for the degree of **Master of Science**.

DATE: ~~July~~ 23, 2003.

## Abstract

In an integrated optical amplifier module, a multiplexer is necessary to combine the signal and pump channels before they are fed to an amplifier. In this thesis a 6X6 pump – signal multiplexer, which can feed an array of six amplifiers simultaneously from a single pump source in an amplifier module is designed. The multiplexer works on the principle of multimode interference and the basic idea in designing the device is to superimpose a signal combiner with a pump splitter in a single structure. The performance of the device was simulated using commercial beam propagation method software. The simulated insertion loss for the signal channel is 0.93 dB and that of the splitter is 0.76 dB. The splitter imbalance is 0.01 dB. An attempt was made to fabricate the device on silicon on insulator material system.

श्री रुक्मिणी सत्यभामा समेत

श्री कृष्ण परमात्मन प्रसादेन मम

सकल कार्य सिध्यर्थम्

श्रीमत् भगवद्गीता स्लोकम

जपम् अहम् गरिष्ये

*By meditating on the sloka of Srimad Bhagavadgeeta, I request the grace of Lord Sree Krishna, who has Rukmini and Satyabhama as forces of thought and action to grant me the success and achievement in every task ahead.*

*For my loving husband Siva*

## Acknowledgements

I would like to express my sincere gratitude to Dr. J. N. McMullin for supervising this thesis work. His patience and kindness during the beginning of my graduate studies are unforgettable. I would also like to thank Dr. C. J. Haugen for his support in carrying out this project. I am thankful to Dr. R. G. DeCorby for the valuable suggestions he made to improve this work.

I would also like to thank Hue Nguyen for helping me in fabricating the device. I am indebted to my fellow graduate students at the TRLabs Edmonton, especially Nakeeran. P, Valerie Hughes and Venkat R. Subramanian for their help in testing the device. The innumerable technical discussions we had were very helpful in understanding many complex concepts in fiber optics. I wish to thank TRLabs Edmonton for providing the necessary financial support and laboratory facilities to carry out this work.

I am indebted to my parents Aruna and Patanjali, my siblings Bhushan and Pani, and my friends Pavani and Kiran for their constant support and love. My special thanks should go to my elder brother Bhushan for making me feel at home here in Edmonton, 12,000 kilometers away from my actual home (Hyderabad, India). I am thankful to my in-laws for their excellent support throughout the two and a half years of my master's work. I would also like to thank my spiritual guru, who showed me a path to the most enthralling subject of Hindu philosophy. I am indebted to my roommate Sirinda and my friend Arun for their kindness during the time of my defense.

Last but not least, I would like to thank my loving husband Siva for his unstinting support and encouragement during the period of my graduate studies. He

supported my decision to continue my education and was ready to stay alone for the course of my work. Without him my graduate studies would not have been possible.

## Table of Contents


Chapter 1 – Introduction ..... 1

1.1. Fiber optic communication systems ..... 1

1.2. WDM components ..... 1

1.3. Optical amplifiers ..... 2

1.4. Photonic integrated circuits ..... 3

1.4.1. Integrated optical amplifier modules ..... 4

1.5. Thesis outline ..... 6

Chapter 2 – Theory of Light Propagation in Waveguides ..... 8

2.1. Total internal reflection (TIR) ..... 8

2.2. Analysis of light propagation in slab waveguide ..... 9

2.3. Rectangular waveguides ..... 12

2.3.1. Electric field in rectangular waveguides ..... 13

2.3.2. Effective index method ..... 14

2.4. Singlemode condition in a rectangular waveguide ..... 15

2.5. Theory of multimode interference ..... 16

2.6. Design technique ..... 25

2.6.1. No field zones ..... 26

2.6.2. Separation between access waveguides ..... 29

2.6.3. Placement of access waveguides ..... 30

Chapter 3 – 6X6 Pump-Signal Combiner: Modeling and Performance ..... 32

3.1. Material system ..... 32

3.2. Silicon on insulator ..... 33

3.3. Access waveguides ..... 35

3.3.1. Singlemode waveguide ..... 35

3.3.2. Separation between access waveguides ..... 37

3.4. Calculating approximate width of the multimode section ..... 39

3.5. Length calculations for the splitter and the coupler ..... 42

3.6. Simulation results ..... 43

Chapter 4 – Device Fabrication ..... 55

4.1. Mask design ..... 55

4.2. Photoresist ..... 56

4.3. Exposing to UV ..... 57

4.4. Etching ..... 58

4.5. Anisotropic silicon dry etching technique - Sidewall passivation ..... 61

Chapter 5 – Device Characterization ..... 66

5.1. Coupling losses ..... 66

5.1.1. Fresnel reflection losses ..... 66

5.1.2. Mode mismatch losses ..... 67

5.2. Scattering losses ..... 69

5.3. Preparing the sample ..... 69

5.4. Experimental setup ..... 70

5.5. Difficulties in testing the device and possible solutions ..... 71

Chapter 6 – Conclusions ..... 74

6.1. Suggested future work ..... 75

6.1.1. Tapered multimode section to reduce the length ..... 75

6.1.2. Pump/Signal combiner as an EDWA gain equalizer ..... 75

References ..... 77

## Table of Figures

Figure 1.1 – Three lower energy levels of erbium ions and various transition processes...3
Figure 1.2– Simplified schematic of a conventional amplifier module ....4
Figure 1.3 – Pump splitter and signal coupler....5
Figure 1.4 –Multiplexer that can feed multiple amplifiers simultaneously....6
Figure 2.1 – Optical fibre ....8
Figure 2.2 – Total internal reflection in a waveguide....8
Figure 2.3 – Planar symmetric slab waveguide....9
Figure 2.4 – Electromagnetic field as a function of $\beta$....11
Figure 2.5a – Rib waveguide....13
Figure 2.5b – Ridge waveguide....13
Figure 2.5c – Embedded waveguide ....13
Figure 2.5d – Channel waveguide ....13
Figure 2.6 – Cross section of a rectangular waveguide....14
Figure 2.7 – Effective index method ....14
Figure 2.8 – Slab coupled waveguide....15
Figure 2.9 – Multimode Interference....17
Figure 2.10 – Multimode interference coupler....18
Figure 2.11 – MMI section with input field and the decomposed mode fields....20
Figure 2.12 – Image positions for a general interference coupler....22
Figure 2.13 – Image positions for a paired interference coupler....23
Figure 2.14 – Image positions for a symmetric interference coupler....24
Figure 2.15a – Ray picture of dead zones ....26
Figure 2.15b – BPM simulation of dead zones ....26
Figure 2.16 – Proposed structure (1) when $L_p > L_s$....27
Figure 2.17 – Proposed structure (2) when $L_p > L_s$....27
Figure 2.18 – Proposed structure (3) ....28
Figure 2.19 – Maximum limit on the $\Delta L$....28
Figure 3.1 – SOI rib waveguide ....33
Figure 3.2 – SOI rib waveguide ....35
Figure 3.3 – Cutoff condition for higher order modes ....36

Figure 3.4 – Field pattern inside the rib waveguide at 1.48 μm ..... 36
Figure 3.5 – BPM simulation of the light propagating inside the waveguide at 1.48 μm. 37
Figure 3.6 – Crosstalk between 100 μm long input waveguides ..... 38
Figure 3.7 – Crosstalk between the pump and signal waveguides. ..... 39
Figure 3.8 – Light propagation inside an S- bend ..... 42
Figure 3.9 – Proposed structure for 6x6 multiplexer ..... 43
Figure 3.10 – Insertion loss sensitivity to the length ..... 44
Figure 3.11 – Crosstalk ..... 46
Figure 3.12 – Sensitivity of insertion loss to the splitter length ..... 47
Figure 3.13a – BPM simulation of the splitter ..... 49
Figure 3.13b – Start and end fields of the splitter ..... 50
Figure 3.14a – BPM simulation of the coupler ..... 51
Figure 3.14b– Field pattern of the splitter ..... 52
Figure 3.15 – Sensitivity of insertion loss to the width variation ..... 53
Figure 3.16 – Coupler performance against varying wavelength ..... 54
Figure 4.1 – Prototype mask ..... 56
Figure 4.2 – Schematic of reactive ion etching ..... 59
Figure 4.3 – Cross sectional view of a rib waveguide ..... 60
Figure 4.4 – Top view of a rib waveguide ..... 60
Figure 4.5 – Cross sectional view of a rib waveguide ..... 62
Figure 4.6a – Side view of rib waveguide ..... 62
Figure 4.6b – Side view of rib waveguide ..... 62
Figure 4.7 – Thickness variation in silicon layer ..... 63
Figure 4.8 – Output section of the multimode waveguide ..... 64
Figure 4.9a – Input section of multimode waveguide ..... 64
Figure 4.9b – Multimode section input layout on the mask ..... 64
Figure 4.10a – Sample edge ..... 65
Figure 4.10b – Rib waveguide ..... 65
Figure 4.11a – Sample edge with no device silicon layer ..... 65
Figure 4.11b – Silicon ridge waveguide ..... 65
Figure 5.1 – Fresnel reflections ..... 67

Figure 5.2a – Longitudinal misalignment ..... 68
Figure 5.2b – Angular misalignment ..... 68
Figure 5.2c – Lateral misalignment ..... 69
Figure 5.3a – Unpolished sample edge ..... 70
Figure 5.3b – Polished sample edge ..... 70
Figure 5.4 – Schematic of experimental set up to characterize the device ..... 70
Figure 5.5 – Photograph of experimental set up to characterize the device ..... 71
Figure 5.6 – Top view of light going through the sample ..... 72
Figure 5.7 – Picture of a sample ..... 73
Figure 6.1 – Access waveguides for efficient coupling ..... 76

## List of Tables

Table 2.1 – Image forming lengths for different interference mechanisms .....24

Table 3.1 – Refractive indices of SOI .....35

Table 3.2 – Effective indices of the waveguide .....37

Table 3.3 – Coupling coefficients for varying separation between two waveguides .....38

Table 3.4 – Calculated lengths of the splitter and coupler for a paired interference device .....40

Table 3.5 – Calculated lengths of the splitter and coupler for a symmetric interference device .....41

Table 3.6a – Splitter insertion losses .....48

Table 3.6b – Coupler insertion losses .....48

Table 4.1 – Silicon etching recipe .....59

Table 4.2 – Silicon etching recipe with sidewall passivating gas .....61

## List of Symbols

| | |
|---|---|
| $c$ | : Velocity of light in vacuum |
| $c_m$ | : Weighting of the mode |
| C | : Complex normalization constant |
| $E$ | : Electric field |
| $E_m$ | : Mode field distribution |
| $h$ | : Height of the core layer outside the rib section |
| $H$ | : Height of the rib section |
| $h_e$ | : Effective height of the core layer outside the rib section |
| $H_e$ | : Effective height of the rib section |
| $J$ | : $\sqrt{-1}$ |
| $k_0$ | : Free space wavevector |
| $K$ | : Coupling coefficient |
| $L_\pi$ | : Beat length of the first two lowest order modes |
| $L$ | : Length of the multimode section |
| $L_p$ | : Length of the pump splitter |
| $L_s$ | : Length of the signal combiner |
| $\Delta L$ | : Length difference between the pump splitter and the signal combiner |
| $m$ | : Number of modes |
| $n_c$ | : Refractive index of the core |
| $n_{ce}$ | : Effective refractive index of the core |
| $n_{cl}$ | : Refractive index of the cladding |
| $n_{cle}$ | : Effective refractive index of the cladding |
| $n_s$ | : Effective refractive index of the core at signal wavelength |
| $n_p$ | : Effective refractive index of the cladding at pump wavelength |
| $N$ | : Number of images |
| $p$ | : Any integer |
| P, Q | : Number of half periods of the mode along y and x directions respectively |
| $P_1$, $P_2$ | : Input and output power |

| | |
|---|---|
| $R$ | : Fresnel reflection coefficient |
| V | : Normalized frequency |
| $W$ | : Width of the waveguide |
| $W_a$ | : Width of the access waveguide |
| $W_e$ | : Effective width of the waveguide |
| $W_s$ | : Separation between the pump and signal access waveguides |
| $\theta_c$ | : Critical angle |
| $\nabla$ | : Laplacian operator |
| $\beta$ | : Propagation constant |
| $\gamma$ | : Attenuation coefficient |
| $\kappa_c$ | : Transverse wave vector in the core |
| $\gamma_{cl}$, $\gamma_c$ | : Attenuation coefficients in cladding and core respectively |
| $\lambda_0$ | : Operating wavelength |
| $\beta_0$, | : Propagation constant of the fundamental mode |
| $\beta_m$ | : Propagation constant of the $m^{th}$ mode |
| $\lambda_p$ | : Pump wavelength |
| $\lambda_s$ | : Signal wavelength |

## List of Abbreviations

| | |
|---|---|
| BESOI | : Bond and etch back method |
| BOE | : Buried oxide etching |
| BPM | : Beam propagation method |
| CD | : Critical dimension |
| $CCl_4$ | : Carbon tetra chloride |
| $CF_4$ | : Carbon tetra flouride |
| CV | : Chemical vapor deposition |
| DWDM | : Dense wavelength division multiplexing |
| EDFA | : Erbium doped fibre amplifiers |
| EDWA | : Erbium doped waveguide amplifiers |
| $H_2O_2$ | : Hydrogen peroxide |
| $H_2SO_4$ | : Sulphuric acid |
| ITU | : International telecommunications union |
| LiNbO3 | : Lithium niobate |
| MMI | : Multimode interference |
| RF | : Radio frequency |
| RIE | : Reactive ion etching |
| SEM | : Scanning electron microscope |
| $SF_6$ | : Sulphur hexa fluoride |
| Si | : Silicon |
| SIMOX | : Separation by implanted oxygen method |
| $SiO_2$ | : Silicon dioxide |
| $SiO_xN_y$ | : Silicon oxynitride |
| SOI | : Silicon on insulator |
| TDM | : Time division multiplexing |
| TE | : Transverse electric |
| TEM | : Transverse electromagnetic |
| TIR | : Total internal reflections |
| TM | : Transverse magnetic |

| | |
|---|---|
| TR*Labs* | : Telecommunications research laboratories |
| WDM | : Wavelength division multiplexing |
| UV | : Ultra violet |

# Chapter 1 – Introduction

## 1.1. Fiber optic communication systems

In a communication system, the information signal is superimposed on an electromagnetic carrier wave. The carrier wave is transmitted to the required destination, where it is demodulated to get the original information signal. Electromagnetic signals at radio, microwave, millimeter wave and optical frequencies are used as carrier frequencies. Higher the frequency of the carrier waves, larger the bit rates it can transmit. Increase in demand for high speed and high bandwidth communication systems led to the development of lightwave communication systems, as the bandwidth capacity of a fiber optic communication system is higher than any other system. In theory, the capacity of an optical fiber can exceed 10 Tb/s. However, the bit rate was limited to 10 Gb/s until 1995 due to the non-linear and dispersive effects of the fiber and the lower speed of electronics. Transmission of multiple channels over a single fiber provided a simpler way of increasing the bit rate beyond 1 Tb/s [1]. Channel multiplexing is achieved with wavelength division multiplexing (WDM) or time division multiplexing (TDM). With the introduction of WDM systems, the state-of the-art fiber optic communications systems are capable of operating at 1.6 Tb/s commercially and 10 Tb/s in labs. Given that the first generation systems had a capacity of 45 Mb/s in 1980, the capacity has grown 10,000 times over a period of 20 years.

## 1.2. WDM components

In WDM systems, each of the data signals is superimposed on a separate wavelength of the light and then jointly led into a fibre optic cable. WDM systems require devices with a greater complexity than systems operating at a single wavelength. Devices such as multiwavelength transmitters and receivers for point-to-point transmission, add-drop multiplexers for coupling one wavelength into and out of a multiwavelength links or ring, and optical crossconnects for wavelength-selective connection of different links or networks are essential in a WDM system. All the passive devices such as multiplexers, demultiplexers, crossconnects and switches introduce losses to the signal and the fiber attenuation also reduces the power level of

the signal. To compensate the signal losses, and make it detectable by the photodetector, optical amplifiers are essential in the system.

### 1.3. Optical amplifiers

Traditionally in long-haul lightwave systems, the signal loss is compensated by using opto-electronic repeaters, in which the optical signal is first converted into an electric signal and then regenerated back to optical signal using a transmitter. These regenerators are quite complex and expensive for a WDM system. An optical amplifier, which amplifies the optical signal without converting it into electrical signal, has proved to be a suitable choice for WDM systems [2]. There are different types of optical amplifiers such as, semi conductor amplifiers (SOA), erbium doped fiber amplifiers (EDFA), Brillouin amplifiers and Raman amplifiers. All these amplifiers increase the power level of the signal by stimulated emission. EDFAs are among the most common due to their ability to simultaneously amplify a number of channels with different bit rates or with different signal formats.

An EDFA consists of a 10 – 30 m long fiber, lightly doped with erbium in which an external light source is employed to amplify the signal with stimulated emission [3]. The three lower energy levels of $Er^{3+}$ ions are shown in Figure 1.1. The ions in the ground state are excited to a higher pump level using pump laser photons. These excited ions decay very quickly to a metastable level (the lifetimes for transitions from this state to the ground state are very long compared to the lifetimes at the pump level). During this decay some of the energy is released as thermal vibrations or phonons. Ions in the metastable state relax to the ground level emitting photons either by spontaneous emission or stimulated emission. Photons emitted by stimulated emission show the same frequency, phase and polarization as that of the triggering information signal photon thus amplifying the signal. Photons emitted by spontaneous emission will have random characteristics and are a source of noise.

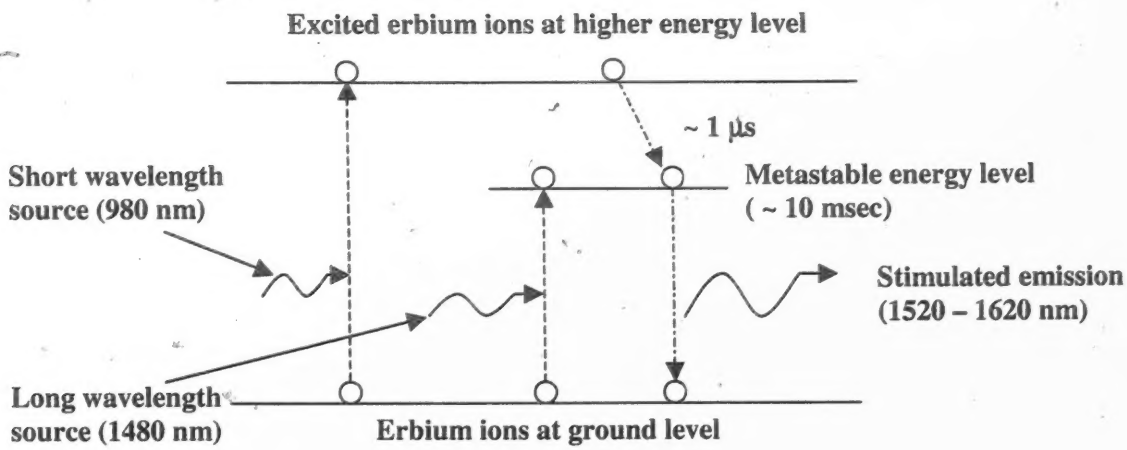


Figure 1.1 – Three lower energy levels of erbium ions and various transition processes

### 1.4. Photonic integrated circuits

The idea of integrated optics was generated about 30 years ago. The motivation behind this idea was to increase the efficiency and reduce the unit cost by miniaturization. In an integrated optics circuit, several optical devices will be placed on a single substrate to perform different tasks. Unlike electronic integrated circuits (IC), photonic integrated circuits are still in the stage of infancy. There are two basic approaches to optical integrated circuits; monolithic integrated circuits and hybrid integrated circuits [4].

In monolithic integrated circuits, all the devices are fabricated on a single semiconductor substrate. This is the same concept used in electronic integrated circuits. However, the fabrication of such circuits is not as easy as it is in electronic ICs since the functionality of each photonic device (laser, amplifier, modulator, splitter or a coupler) shows optimal performance in a different material. In order for monolithic integrated circuits to be successful, a single material that provides multiple functionalities must be found.

Hybrid integrated circuits avoid the major problem faced by monolithic integration. In hybrid integrated photonic circuits a substrate material is chosen and different devices are mounted on it. The individual devices of the circuit can be fabricated using optimal material for its functionality. The main problem with this type

of integration is the efficient alignment of the different optical components, which is essential for having low coupling losses between the components.

### 1.4.1. Integrated optical amplifier modules

Generally, the EDFAs are not small devices and it is difficult to integrate them with other photonic devices. In view of integrated photonic circuits, planar versions (erbium doped waveguide amplifiers-EDWA) of EDFA are being developed in which the amplifiers are in the form of planar waveguides [5],[6].

Currently, many integrated optical device modules such as amplifiers [7], [8], modulator [9], and photodetectors [10] are commercially available. In an optical amplifier module, it is necessary to have a multiplexer, which combines the signal and pump channels, before they are fed to the amplifier. Figure 1.2 shows a simplified picture of conventional amplifier module architecture.

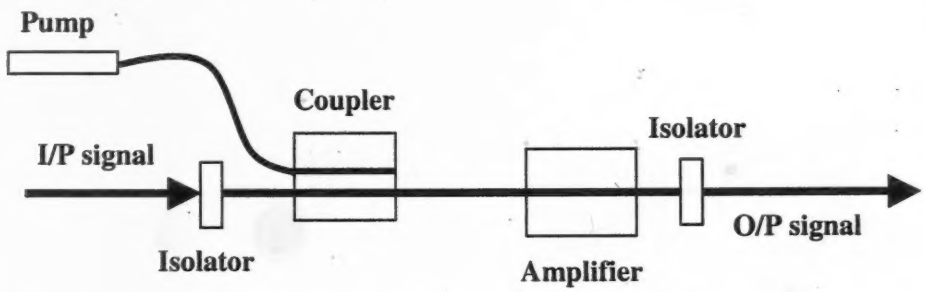


Figure 1.2 – Simplified schematic of a conventional amplifier module

To lower the cost of amplifier modules in a WDM metropolitan node structure, novel multiport EDFA architectures have been developed [11]. Some commercially available versions employ amplifier banks[12]. For these architectures it is highly desirable to have a combiner, which can combine multiple signals with the pump and feed the amplifiers simultaneously. This thesis work was carried out in this relatively unexplored area of research.

Traditionally, directional couplers [13],[14] are used to combine the pump and signal channels before they enter the amplifier. In spite of their simplicity in modeling, they are sensitive to the fabrication tolerances and show more losses. There are other options such as two-mode interference couplers [15], Mach-Zehnder interferometers

[16], and asymmetric Y-junctions [17]. Devices based on these methods are usually very long, which may not be suitable for an integrated optics circuit. The asymmetric Y-junction devices demand a complex fabrication process.

Devices based on multimode interference mechanism have also been used as multiplexers [18]. The MMI devices used for combining the pump and signal channels have one channel in cross-coupled position and the other one in bar coupled position. The MMI devices are proved to be fabrication tolerant [19], polarization insensitive [20] and show low losses. All of these properties are highly desirable for an integrated multiplexer.

A multimode multiplexer that can feed two amplifiers simultaneously was developed at the TR*Labs* Edmonton previously [21]. By employing this device in an integrated amplifier module, the cost and complexity of the module is expected to be reduced considerably. The basic idea in realizing this device is to superimpose a pump splitter with a signal combiner (Figure 1.3). The width of the splitter and combiner is the same and the length of each device is chosen such that they closely match. By exploiting the no field zones at the input of the multimode waveguide, two devices with different lengths are superimposed in a single structure.

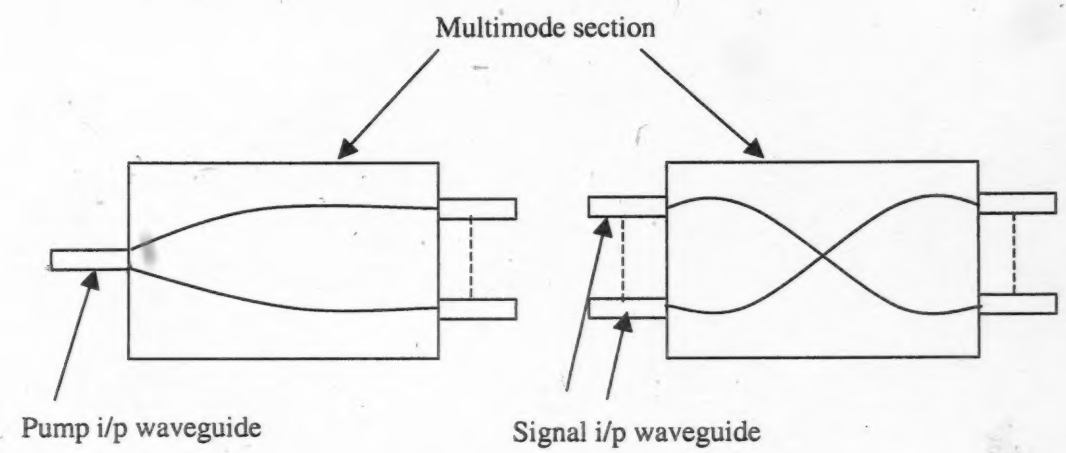


Figure 1.3 – Pump splitter and signal coupler

As an extension to this work, using the same concept, a multiplexer that can feed six amplifiers simultaneously (Figure 1.4) was modeled in this thesis. The device modeling is primarily based on multimode interference.

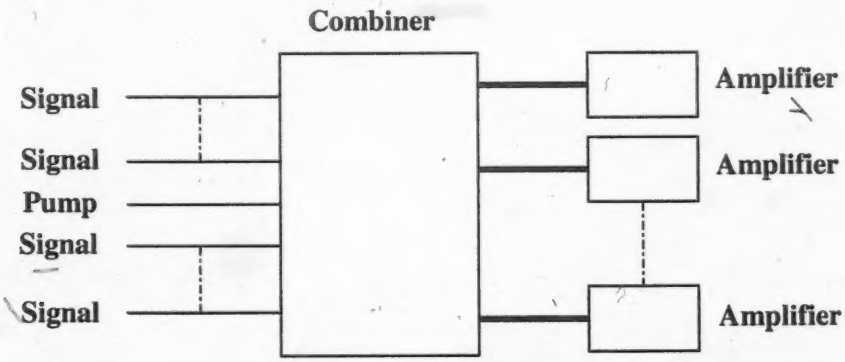


Figure 1.4 – Multiplexer that can feed multiple amplifiers simultaneously

## 1.5. Thesis outline

Chapter 2 introduces the basic concepts of light propagation and field solutions in rectangular waveguides. Effective index method and singlemode condition in rectangular waveguides are discussed. Principles of self-imaging or MMI and different types of imaging techniques are also explained in this chapter. In the last section, the device designing technique is described.

In Chapter 3, the properties of the Silicon on Insulator material (SOI) system are discussed. Taking into account the material constants of the SOI, the singlemode condition for access waveguides is plotted. Based on the access waveguide dimensions and the separation between them, the device dimensions are calculated following the device designing technique explained in Chapter 2. Some of the device simulation results are also presented in this chapter. Difficulties in optimizing the dimensions are discussed.

Chapter 4 discusses the device fabrication procedure. Silicon etching methods and difficulties in achieving the sidewall smoothness are explained. As a solution to the anisotropy in the rib height, sidewall passivation schemes are considered. Finally, some Scanning Electron Microscope (SEM) pictures of the fabricated device are presented.

Chapter 5 deals with the device testing. Different loss mechanisms in device characterization are discussed. Difficulties in conducting the experiment are also explained briefly.

In Chapter 6 some concluding ideas and recommended future work are presented.

## Chapter 2 – Theory of Light Propagation in Waveguides

### 2.1. Total internal reflection (TIR)

Transmission of light through a dielectric waveguide was first proposed in the beginning of 20th century. A dielectric waveguide guides light from one point to another point. An optical fiber (Figure 2.1) serves as a common example for a dielectric waveguide.

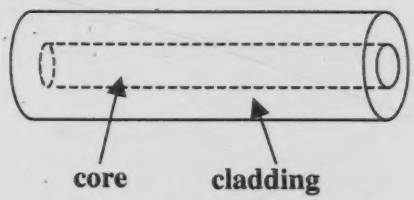


Figure 2.1 – Optical fibre

Light is confined and guided in the waveguide due to a phenomenon called total internal reflection (TIR) [22]. TIR allows the rays to completely reflect at the dielectric interface with no light escaping out from the dielectric. The light rays bounce back and forth at the dielectric interface and travel inside the waveguide. Figure 2.2 illustrates total internal reflection, using ray optics in a dielectric slab waveguide.

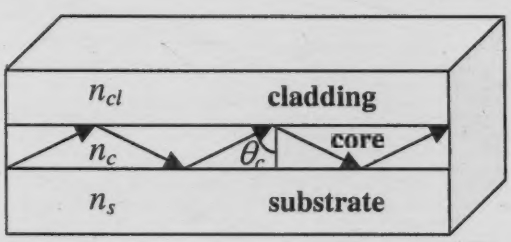


Figure 2.2 – Total internal reflection in a waveguide

To obtain the total internal reflection of light at the interface of two dielectric materials, the following conditions must be met:

[1]. Core refractive index must be greater than that of the substrate and cladding. That is $n_c > n_s, n_{cl}$, where $n_c$ is the core refractive index, $n_{cl}$ is the cladding refractive index and $n_s$ is the substrate refractive index.

[2]. The angle of incidence should be greater than the critical angle given by $\theta_c$, where $\theta_c = \sin^{-1}(\frac{n_{cl}}{n_c})$ at the core-cladding interface and $\theta_c = \sin^{-1}(\frac{n_s}{n_c})$ at the core-substrate interface.

## 2.2. Analysis of light propagation in slab waveguide

A slab waveguide (Figure 2.3) is a 3 dimensional planar waveguide with infinite width and length when compared to the wavelength of the light. It consists of a light guiding material or core (refractive index $n_c$) sandwiched between an upper cladding (refractive index $n_{cl}$) and a lower cladding or substrate (refractive index $n_s$).

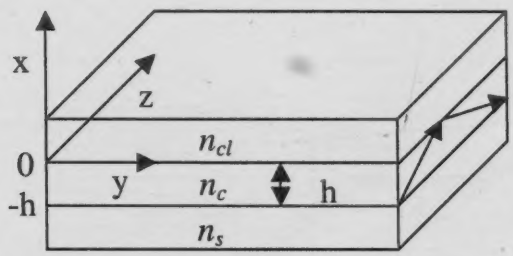


Figure 2.3 – Planar symmetric slab waveguide

Consider the complex wave equation for the electric field assuming the wave is traveling in positive z direction.

$$\nabla^2 E - \frac{n^2}{c^2}\frac{\partial^2 E}{\partial t^2} = 0, \tag{2.1}$$

where $\nabla^2$ is the Laplacian operator defined as $\left(\frac{\partial^2}{\partial x^2}+\frac{\partial^2}{\partial y^2}+\frac{\partial^2}{\partial z^2}\right)$, $c$ is the velocity of light in vacuum, $n$ is the refractive index of the medium and $E$ is the electric field. The field $E$ can be transverse electric (TE) or transverse magnetic (TM) or hybrid transverse electromagnetic (TEM), depending on the orientation. In the TE case, the electric field is polarized along the y-axis and in the TM case, it is polarized along the x-axis. Throughout this thesis it is assumed that the light is TE polarized and propagates in the z-direction.

Equation 2.1 is a vector wave equation. It can be simplified by rewriting in terms of the components of the field. In rectangular coordinates, the vector Laplacian is written as three uncoupled components. For a sinusoidal wave with angular frequency $\omega$, the wave equation for the electric field components in each region can be put in scalar form. For a TE polarized field, the scalar field equation is given by,

$$\nabla^2 E_y + k_0^2 n_i^2 E_y = 0 \tag{2.2}$$

where $k_0$ is the vacuum wavevector given by $\frac{2\pi}{\lambda}$ and

$$n_i = \begin{cases} n_c & -h < x < 0; \\ n_s & x < -h; \\ n_{cl} & x > 0; \end{cases} \quad \text{(Figure 2.3).} \tag{2.3}$$

Since it is assumed that the length and the width of the waveguide are infinite, there will be a translational invariance in the z and y-directions. However, it is expected that there will be some phase accumulation in the direction of propagation. Considering these conditions, the general solution takes the form

$$E_y(x,z) = E_y(x) e^{-j\beta z}, \tag{2.4}$$

where $\beta$ is called the longitudinal wavevector or propagation constant.
Substituting Equation 2.4 into Equation 2.2 gives

$$\frac{\partial^2 E_y(x)}{\partial x^2} + \left(k_0^2 n_i^2 - \beta^2\right) E_y(x) = 0. \tag{2.5}$$

The general solution of Equation 2.5 is of the form,

$$E_y(x) = E_0 e^{\pm\left(\sqrt{\beta^2 - k_0^2 n_i^2}\right)x}. \tag{2.6}$$

Equation 2.6 represents a mode field equation. Each value of $\beta$ represents a unique mode and each of the modes will have a unique field distribution. The value of $k_0^2 n_i^2 - \beta^2$ determines if the mode is guided. There are two possible cases.

First, $k_0^2 n_i^2 - \beta^2 < 0$, then the field $E_y(x)$ is given by

$$E_y(x) = E_0 e^{-\gamma x}. \tag{2.7}$$

In this case, the wave is exponentially decaying and $\gamma$ is called the attenuation coefficient.

Second, $k_0^2 n_i^2 - \beta^2 > 0$, then the field solution is oscillatory in the transverse direction of the waveguide.

For a mode to be guided, Equation 2.6 should satisfy evanescent conditions in the cladding and substrate regions and, oscillatory solutions in the core region.

Hence, in substrate and cladding regions

$$k_0^2 n_s^2 < \beta^2, \text{(Assuming } n_s > n_c\text{)} \tag{2.8a}$$

and in core region

$$k_0^2 n_c^2 > \beta^2 . \tag{2.8b}$$

Combining the Equations 2.8a and 2.8b gives the condition for a mode to be guided as

$$k_0 n_s < \beta < k_0 n_c . \tag{2.9}$$

Figure 2.4 illustrates the mode guiding conditions pictorially [22] (First two modes are not guided and the last mode is guided).

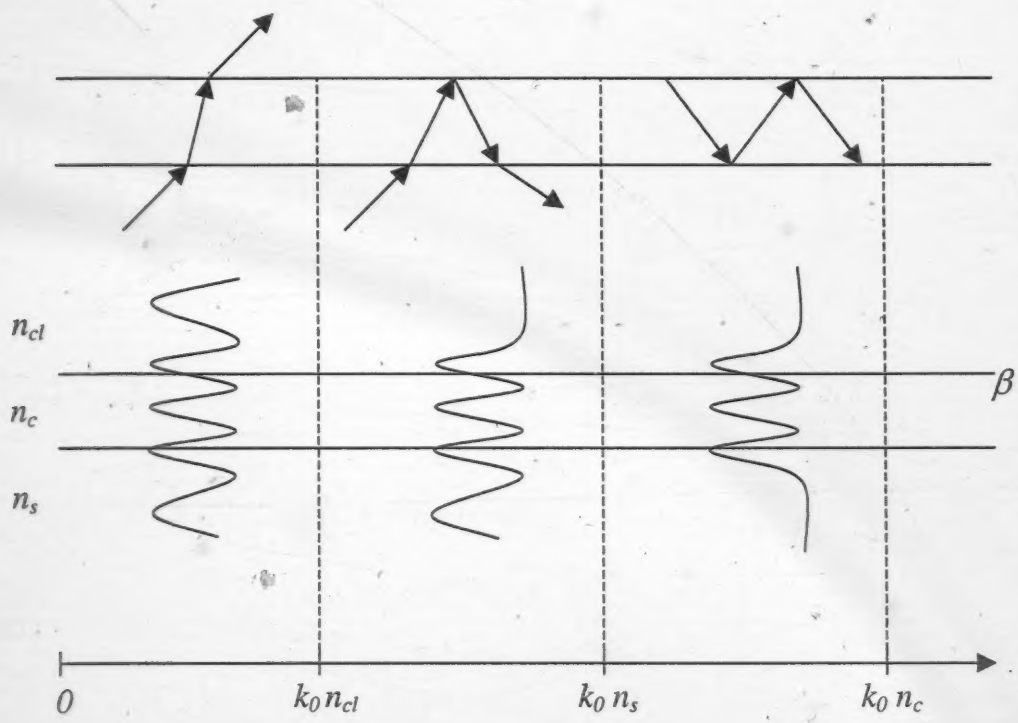


Figure 2.4 – Electromagnetic field as a function of $\beta$

The value of $\beta$ is determined by applying boundary conditions to the general solution given by Equation 2.6, which gives the following transcendental equation

$$\tan(h\kappa_c) = \frac{\gamma_{cl} + \gamma_s}{\kappa_c\left[1 - \frac{\gamma_{cl}\gamma_s}{\kappa_c^2}\right]}, \tag{2.10}$$

where $\gamma_{cl}$ is the attenuation coefficient in cladding, $\gamma_s$ is the attenuation coefficient in the substrate region, $h$ is the core thickness and $\kappa_c$ is the transverse wave number given by

$$\kappa_c = \sqrt{k_0^2 n_i^2 - \beta^2}\,. \tag{2.11}$$

Equation 2.10 is known as the characteristic equation for TE modes and it can be solved either graphically or numerically to get the value of $\beta$ for each mode.

Waveguides are usually characterized by the number of guided modes. It is necessary to determine the number of modes in a waveguide, as the properties of single and multimode waveguides vary greatly. The number of guided modes $m$ in a waveguide is approximated by

$$m = Int\left(\frac{V}{\pi}\right), \tag{2.12}$$

where $V$ is called the normalized frequency and is defined as $hk\sqrt{(n_c^2 - n_s^2)}$.

## 2.3. Rectangular waveguides

The slab waveguide is an idealization of a practical waveguide. In slab waveguides, light is confined in only one direction and as a result, most of the energy leaks out resulting in lossy waveguides. By tailoring the shape and structure of the waveguide, it is possible to confine light in both the x and y-directions. In Figure 2.5, different types of waveguides are shown. Essentially, in all these waveguides light is confined in the core material in two directions x and y and travels in the z-direction.

Figure 2.5a – Rib waveguide

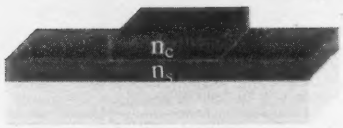


Figure 2.5b – Ridge waveguide

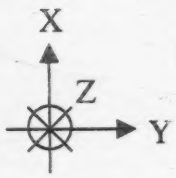


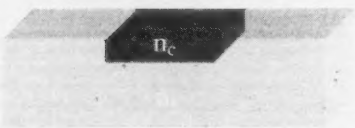


Figure 2.5c – Embedded waveguide

Figure 2.5d – Channel waveguide

### 2.3.1. Electric field in rectangular waveguides

Figure 2.6 shows the cross section of a rectangular waveguide. Unlike in slab waveguides, the field is a function of both x and y in rectangular waveguides. The major difficulty in analyzing this structure lies in the corner regions. Mode fields in these areas are strongly coupled in x and y-directions. Well above the cutoff ($m\pi << V < (m+1)\pi$), the field in corner regions can be assumed negligible and the solutions are analytically tractable. If this coupling is neglected, the mode equation can be separated into uncoupled solutions $E_x(x)$ and $E_y(y)$. However, solving the two dimensional mode field equations analytically is very tedious and for some of the practical structures, analytical solutions do not exist. In these cases the Maxwell's equations are solved using numerical methods such as, finite difference method, finite element method and finite difference beam propagation method [23]. The numerical techniques yield accurate results at the expense of computational complexity. Semi-analytical methods such as Marcatili's method [24], spectral index method [25] and effective index method [26], [27], are also used in solving the mode field equations. Semi-analytical methods make certain approximations to the structure under consideration and then solve the resulting simplified problem analytically.

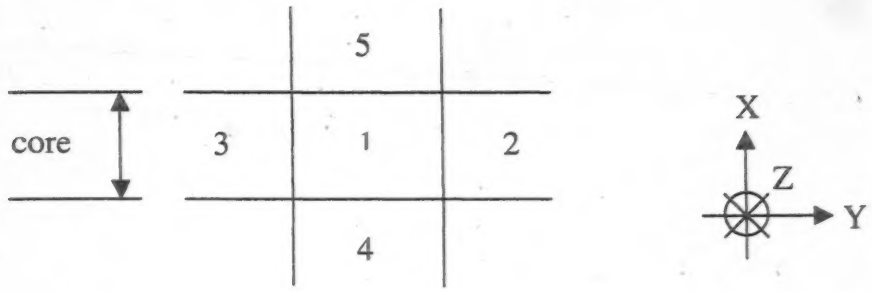


Figure 2.6 – Cross section of a rectangular waveguide

### 2.3.2. Effective index method

The effective index method is one of the widely used semi-analytical methods to solve the field equations in a rectangular waveguide. This technique replaces the rectangular structure with an equivalent slab structure with effective indices. The rib waveguide structure is divided into three parts as shown in the Figure 2.7 and each part is considered as a slab waveguide. The fundamental vertical indices are calculated using the slab waveguide transverse wave equations. The resulting effective indices are considered as the refractive indices for the vertical slab as shown in Figure 2.7. The wave equation for symmetric slab waveguide is solved to get the final mode field solutions. The effective index method produces accurate results but it overestimates $\beta$ near cutoff.

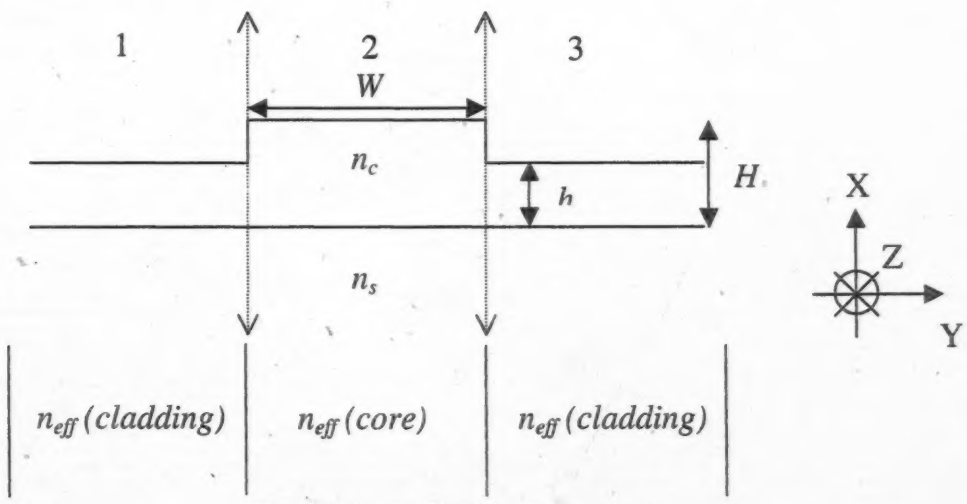


Figure 2.7 – Effective index method

## 2.4. Singlemode condition in a rectangular waveguide

The effective index method provides a very simple condition for singlemode propagation in large cross section rib waveguides [28]

$$t < \frac{r}{\sqrt{1-r^2}} \qquad for \quad r > 0.5, \tag{2.13}$$

where $t = \frac{W_e}{H_e}$, $r = \frac{h_e}{H_e}$, $h_e = h + q$, $H_e = H + q$, $W_e = W + 2\frac{p_{cl}}{k_0\sqrt{(n_c^2 - n_{cl}^2)}}$,

$q = \frac{p_{cl}}{k_0\sqrt{(n_c^2 - n_{cl}^2)}} + \frac{p_s}{k_0\sqrt{(n_c^2 - n_s^2)}}$, and $p_{cl}, p_s = 1$ for TE modes.

Many other theories [29], [30] were developed with small changes in the original effective index method for more accurate singlemode condition. However, all these methods are valid only when $r > 0.5$.

Singlemode condition for $r < 0.5$ can be obtained by following the slab coupled waveguides theory as explained by Marcatili [31]. In this analysis the rib structure is assumed as a dielectric rod lying on top of a slab waveguide, which covers the substrate as shown in Figure 2.8. Assume that the rib section supports $m$ modes and the slab section supports $r$ modes. Modes with same propagation constant, couple energy to each other between slab and the rib section. Hence, these modes will travel without any attenuation due to the coupling. Other modes that are excited in the rib section but not in the slab section, couple energy to the modes in slab section.

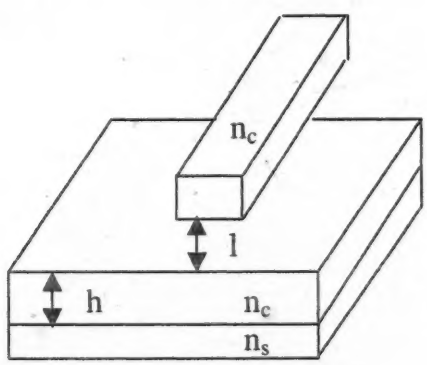


Figure 2.8 – Slab coupled waveguide

As a result, these modes attenuate after traveling some distance. Thus, it is possible to determine the number of lossless modes in the rib section by adjusting the thickness of the slab and hence the number of modes in it.

Considering the complicated mathematics involved in the analysis, only the results are presented here. The dimensions of a waveguide at which mode $E_{PQ}$ is cut off is determined by

$$\frac{Ph_e}{W_e} - \sqrt{1-\left(\frac{Qh_e}{H_e}\right)^2} = \frac{2}{\pi}\frac{h_e^2}{W_e H_e}, \tag{2.14}$$

where $P$ and $Q$ are number of half periods of the mode along $y$ and $x$ directions respectively. Equation 2.14 is plotted with $\frac{h_e}{W_e}$ *and* $\frac{h_e}{H_e}$ as variables. The coordinates of the curve yield the smallest possible values of ratios $\frac{h_e}{W_e}$ *and* $\frac{h_e}{H_e}$ for the mode $E_{PQ}$ to be cut off.

A waveguide is singlemoded if the modes $E_{12}$ and $E_{21}$ are cut off. To determine the dimensions of the waveguide at which the $E_{12}$ and $E_{21}$ modes are cut off, Equation 2.14 needs to be plotted for two sets of parameters $P=1,\ Q=2$ *and* $P=2,\ Q=1$. These curves yield the smallest possible dimensions of the waveguide for singlemode operation. This approach was employed in designing singlemode access waveguides and described in Section 3.3.

## 2.5. Theory of multimode interference

Multimode interference (MMI) was initially described by Bryngdahl [32] and Ulrich [33]. MMI or self-imaging is a unique property of multimode waveguides and can be defined as "*The property of multimode waveguides by which the input field profile is reproduced at regular intervals along the direction of light propagation*" [34]. Figure 2.9 shows the simulated field distribution inside a multimode waveguide. Light is sent through an input access waveguide to the multimode waveguide. Images of the input field are formed along the length of the waveguide at regular intervals. Multiple and single images can also be seen in the picture.

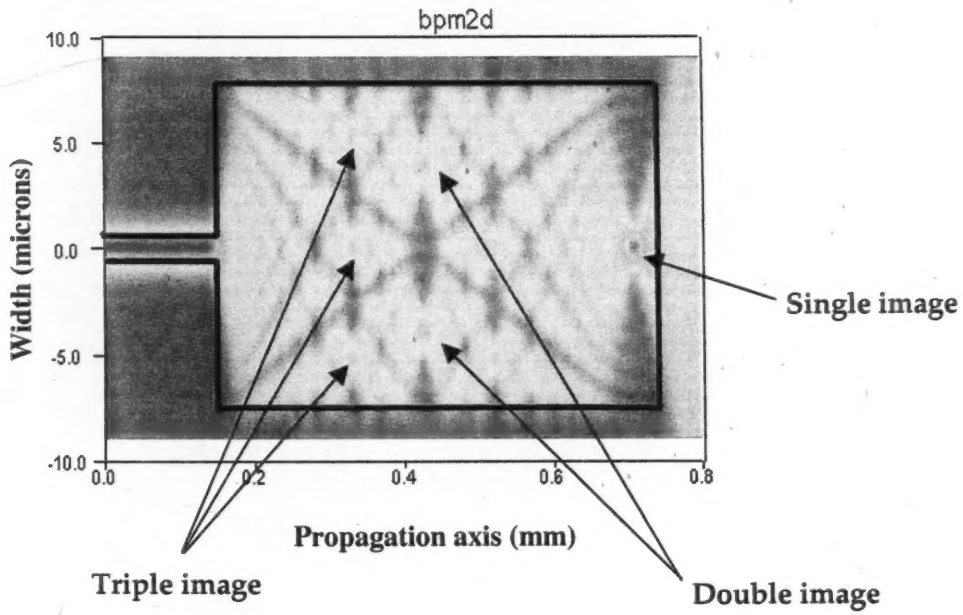


Figure 2.9 – Multimode Interference

The principle of self-imaging can be understood as follows. At the input of the multimode section, the field can be expressed as the superposition of the weighted guided modes, assuming the input field excites only guided modes. After traveling a fixed distance each mode will accumulate a different phase, due to the varying propagation constants ($\beta$) for each guided mode. Thus, at an arbitrary distance in the waveguide, superposition of all the modes will not yield a faithful reproduction of the input field profile. However, at beat lengths, where the phase difference between different modes equals an integral multiple of $2\pi$, the superposition of some or all of the modes will reconstruct the input field. (Images can be multiple or single depending on the number of modes that beat together). As a rule of thumb, m+1 number of modes is required to be excited in the multimode waveguide to form m images [34].

Consider a multimode rib waveguide of width $W$ that can guide $m$ number of modes in the y-direction and a singlemode in x-direction (Figure 2.10). A number of access rib waveguides are connected to the multimode waveguide, at equal distances from each other to couple light into and out of the multimode section. Using the effective index method (Section 2.3.2) the rib structure is reduced to an equivalent slab

structure with effective indices. Throughout this thesis, the effective indices of the core and cladding are referred to as $n_{ce}$ and $n_{cle}$ respectively.

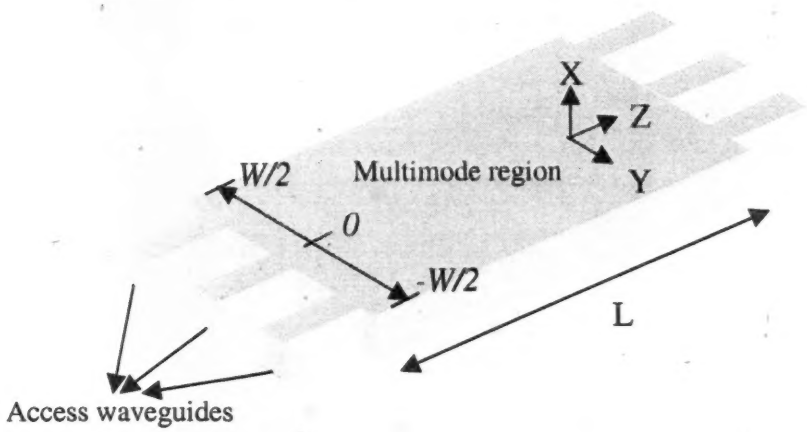


Figure 2.10 – Multimode interference coupler

If the index contrast between the cladding and the core is small, the modal fields penetrate deeply into the cladding and the effective width of the waveguide is larger than the physical width $W$. The effective width of the waveguide $W_e$, is given by the following equation,

$$W_e = W + \left(\frac{\lambda_0}{\pi}\right)\left(\frac{n_{cle}}{n_{ce}}\right)^{2\sigma} \frac{1}{\sqrt{n_{ce}^2 - n_{cle}^2}}, \tag{2.15}$$

where $\lambda_0$ is the operating wavelength and $\sigma = 0$ for TE modes [35]. In high index contrast waveguides the field will be tightly confined within the waveguide, resulting in a small penetration depth which allows $W$ to be approximately equal to $W_e$.

Consider a field $E_y(y)$ fed to the multimode section through an input waveguide. The field distribution at any distance z along the waveguide is then given by the superposition of all the guided modes in the waveguide. Assuming that only guided modes are excited, the input field can be expressed as a sum of the mode fields

$$E_y(y,0) = \sum_0^m c_m \mathrm{E}_m(y), \tag{2.16}$$

where $\mathrm{E}_m(y)$ is the mode field distribution and $c_m$ determines the weighting of each mode given by the overlap coefficient

$$c_m = \frac{\int E_y(y,0)\mathrm{E}_m(y)dy}{\sqrt{\int \mathrm{E}_m^2(y)dy}}. \tag{2.17}$$

The field distribution at any distance z is given by,

$$E_y(y,z) = \sum_0^m c_m \mathrm{E}_m(y)\mathrm{e}^{j(\omega t-\beta_m z)}. \tag{2.18}$$

Assuming that the time dependence is implicit and taking the fundamental mode phase factor as a common factor, the field distribution assumes the form,

$$E_y(y,z) = \sum_0^m c_m \mathrm{E}_m(y)\mathrm{e}^{j(\beta_0 z-\beta_m z)}. \tag{2.19}$$

For the Equation 2.19 to exactly represent the input field, the following conditions must be met

$$e^{j(\beta_0-\beta_m)z} = 1 \ or \ (-1)^m. \tag{2.20}$$

When the first condition of Equation 2.20 is satisfied, the phase changes of the modes differ by integer multiples of $2\pi$ and the images formed are direct images. If the phase changes are alternatively even and odd multiples of $\pi$, the images formed are mirrored. For practical purposes, it is very convenient to express modal propagation constants in terms of the physical features of the waveguide.

The two transverse components of the wavevector, transverse propagation constant $\kappa_m$ and longitudinal propagation constant $\beta_m$ are related by the dispersion equation (Equation 2.10)

$$k_0^2 n_{ce}^2 = \beta_m^2 + \kappa_m^2, \tag{2.21}$$

Strongly guided modes are completely confined within the waveguide. As a result the transverse profile of a strongly guided mode will contain an integral multiple of half-periods within the waveguide. Thus the transverse propagation constant is given by

$$\kappa_m = \frac{(m+1)\pi}{W_e}. \tag{2.22}$$

The corresponding longitudinal propagation constant can be obtained by solving Equation 2.21, using the paraxial approximation and binomial expansion,

$$\beta_m \simeq k_0 n_{ce} - \frac{(m+1)^2 \pi \lambda_0}{4 n_{ce} W_e^2}. \tag{2.23}$$

From Equation 2.23, the propagation constant spacing between modes is given by

$$\beta_0 - \beta_m \simeq \frac{m(m+2)\pi}{3L_\pi}, \tag{2.24}$$

where $L_\pi$ is the beat length of the first two lowest order modes and is given by

$$L_\pi = \frac{4 n_{ce} W_e^2}{3\lambda_0}. \tag{2.25}$$

Substituting Equation 2.24 into Equation 2.20 results in

$$L = p(3L_\pi) \qquad for \quad p = 1, 2, 3, 4... \tag{2.26}$$

where $L$ is the length at which the image is formed and the factor $p$ represents the periodicity of the image formation. Direct images are formed when $p$ is an even number and mirrored images are formed when $p$ is an odd number. Multiple images are formed at intermediate positions along the length of the multimode waveguide.

Analytical expressions for the positions and phases of the multiple images have been obtained by using Fourier analysis and the properties of generalized gaussian sums [36]. A brief summary of the assumptions in deriving the lengths at which multiple images are formed, and the results are given in the following. To simplify the problem, a virtual MMI section with a width $W$ is added to the real section as shown in Figure 2.11.

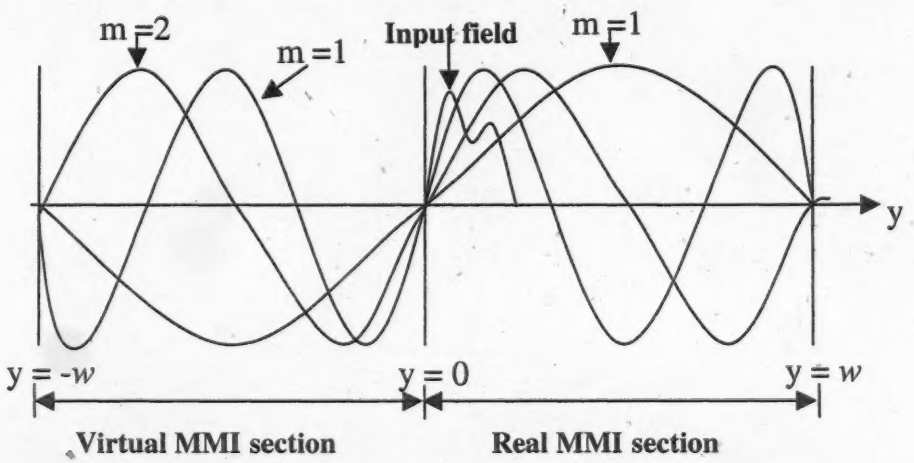


Figure 2.11 – MMI section with input field and the decomposed mode fields

The input field in the real section is extended to the virtual section forming an antisymmetric function $E_{in}(y)$. Hence, the mode field amplitudes can be approximated by sine functions. That is $E_m(y) \simeq \sin(\kappa_m y)$.

Based on these conditions it is obtained that, at a length

$$L = \frac{p}{N}(3L_\pi) \tag{2.27}$$

where, $p$ and $N$ are two integers with no common divisors, the field can be put in the form

$$E(y, L) = \frac{1}{C}\sum_{q}^{N-1} E_{in}(y - y_q)e^{j\phi}, \tag{2.28}$$

with $y_q = p(2q - N)\frac{W_e}{N}$, and $\phi = p(N - q)\frac{q\pi}{N}$.

Here $q$ refers to each of $N$ images, $y_q$ refers to the position of the image, $\phi$ is the phase, and $C = \frac{1}{\sqrt{N}}$ is the complex normalization constant. Equation 2.28 shows that at a length $L$ defined by Equation 2.27, $N$ images are formed at the defined positions. The optical phases of the each self image is given by

$$\begin{aligned} \phi_{ij} &= \frac{\pi}{4N}(j-1)(2N+i-j)+\pi \quad \textit{for } i+j \textit{ even}, \\ \phi_{ij} &= \frac{\pi}{4N}(i+j-1)(2N-i-j+1) \quad \textit{for } i+j \textit{ odd}, \end{aligned} \tag{2.29}$$

where $i$ = *1,2,3,4.....N* is the bottom-up numbering of the input waveguides and $j$ = *1,2,3,4.....N* is the top-down numbering of the output waveguides as shown in Figure 2.12.

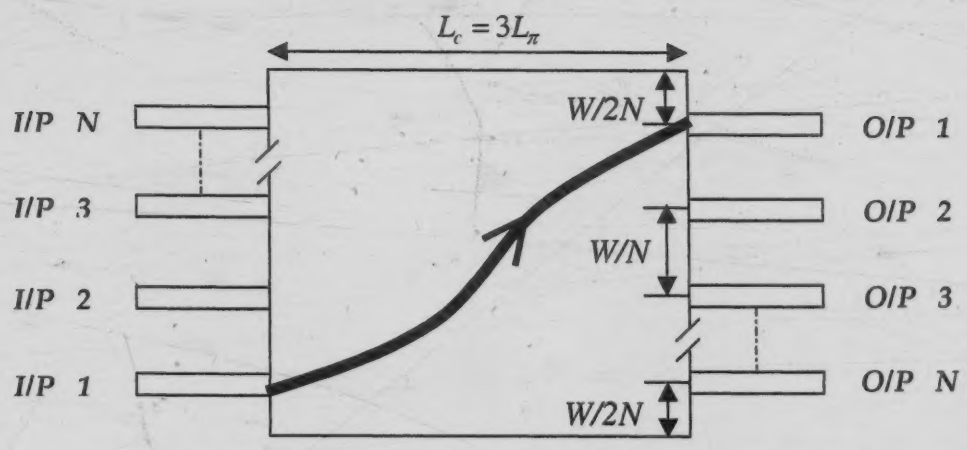


Figure 2.12 – Image positions for a general interference coupler

So far in the analysis, selective excitation of modes is not considered. It is assumed that all the modes that can be guided by the multimode section are excited and this condition is called *'general interference'*. However, it is possible to excite only desired modes. Depending on the modes that are excited, the lengths at which the images are formed will vary and this condition is called *'restricted interference'* or *'overlapping imaging'* [37].

If the modes numbered m = 2,5,8... are not excited, the length periodicity of the image formation is reduced by a factor of 3 and the method is known as *'paired interference'*. This selected excitation is achieved by placing the input waveguides at positions $\pm\frac{W_e}{6}$, where the modes numbered 2,5,8... have nodes. Figure 2.13 shows the positions of the images for paired interference mechanism.

The length at which a single image is formed is given by

$$L = p(L_\pi), \tag{2.30}$$

and multiple images are formed at

$$L = \frac{p}{N}(L_\pi). \tag{2.31}$$

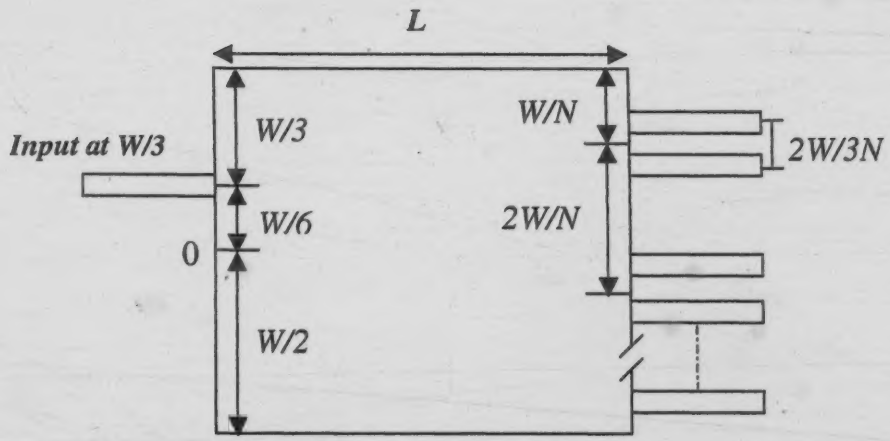


Figure 2.13 – Image positions for a paired interference coupler

It is also possible to excite only the even modes by center feeding the input of the multimode waveguide with a symmetric input field. This is called the '*symmetric interference*' mechanism. In this case single images are formed at

$$L = \frac{3}{4} p(L_\pi), \tag{2.32}$$

and multiple images are formed at

$$L = \frac{3p}{4N}(3L_\pi). \tag{2.33}$$

This is a length reduction of 4-times compared to general interference. Figure 2.14 shows the image positions for a symmetric interference coupler. Table 2.1 summarizes the image forming lengths with different interference mechanisms.

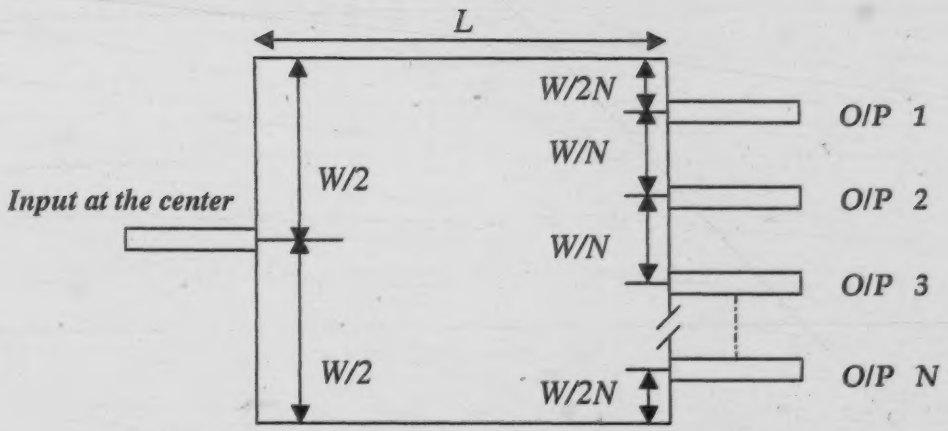


Figure 2.14 – Image positions for a symmetric interference coupler

| | General interference | Paired interference | Symmetric interference |
|---|---|---|---|
| Beat length | $L_\pi = \frac{4n_{ce}W_e^2}{3\lambda}$ | $L_\pi = \frac{4n_{ce}W_e^2}{3\lambda}$ | $L_\pi = \frac{4n_{ce}W_e^2}{3\lambda}$ |
| Length at which single image formed | $L = 3p(L_\pi)$ | $L = p(L_\pi)$ | $L = \frac{3}{4}p(L_\pi)$ |
| Length at which multiple images formed | $L = \frac{3}{N}p(L_\pi)$ | $L = \frac{p}{N}(L_\pi)$ | $L = \frac{3}{4}\frac{p}{N}(L_\pi)$ |

Table 2.1 – Image forming lengths for different interference mechanisms

In reality, the images will be formed at distances deviated from the theoretical values because the quadratic dependence of $\beta$ with the mode number (Equation 2.23) is an approximation. Thus, in modeling the devices based on MMI, it is essential to simulate the device using beam propagation techniques (BPM) [38], [39] before it is actually fabricated. The device in this thesis is designed using commercial BPM software called Olympios [40]. Wide angle BPM based on Pade approximations [41],

[42] was used to design the device for accurate results at a higher index contrast of the core and cladding.

## 2.6. Design technique

Objective of this work is to design a combiner that can feed multiple amplifiers simultaneously from a single pump source. This can be achieved by superimposing a pump splitter with a signal combiner (Figure 1.3) [21]. The superimposed single structure is able to split the pump channel into multiple channels and combine these pump channels with the signal channels.

The multimode interference technique described previously (Section 2.5), is used to design the device. In this design, the length of the multimode section is chosen such that the pump input forms multiple images at the output plane of the multimode waveguide, and each of the signal input forms a single image at the output plane. The images formed are coupled into singlemode output waveguides, which are connected to the amplifiers. Thus each output will carry $1/N^{th}$ of the pump power and a signal channel, where $N$ is the number of pump images.

Assume that the signal combiner length is $L_s$ (Equation 2.26) and the pump splitter length is $L_p$ (Equations 2.31 and 2.33). Let the pump and signal wavelengths are $\lambda_p$ and $\lambda_s$ respectively. Also assume that the core effective indices of the waveguide are $n_p$ and $n_s$ at pump and signal wavelengths respectively. To superimpose the splitter and coupler in a single structure, $L_p$ should be equal to $L_s$, that is,

$$\frac{p}{N}\frac{n_p}{4\lambda_p} = \frac{n_s}{\lambda_s} \qquad \text{(For symmetric interference splitting)} \qquad (2.34a)$$

and

$$\frac{p}{N}\frac{n_p}{\lambda_p} = 3\frac{n_s}{\lambda_s} \qquad \text{(For paired interference splitting)} \qquad (2.34b)$$

By choosing suitable values for $p$, $n_s$ and $n_p$ it is possible to have the same length for splitter and coupler. However, it is not always possible to satisfy the Equation 2.34 in which case, the input regions of the MMI where the filed intensity is very low is exploited to makeup the length difference [21].

### 2.6.1. No field zones

Consider a multimode waveguide with a singlemode input waveguide. The field pattern inside the multimode waveguide is shown in the following figures

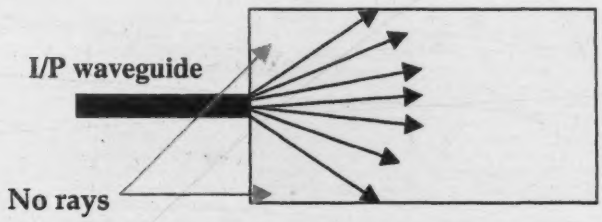


Figure 2.15a – Ray picture of dead zones

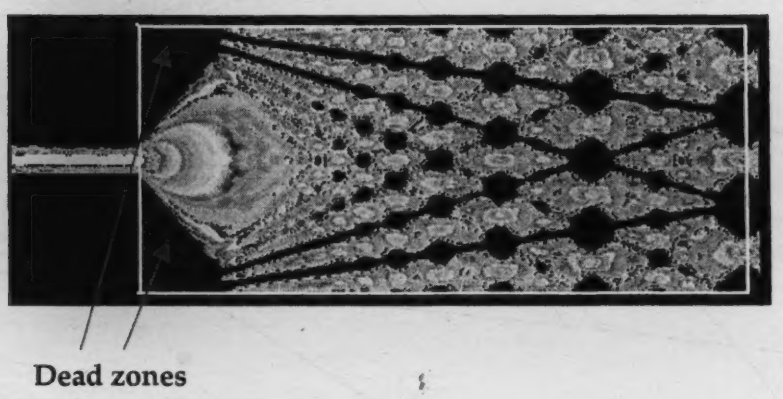


Figure 2.15b – BPM simulation of dead zones

All of the rays that are issuing out of the single mode waveguide must hit the multimode waveguide core-cladding interface at angles greater than critical angle. Hence, at the input section of multimode waveguide there will be no field in the corners. The naturally tapered shape of the field at the beginning of the multimode section can be exploited to superimpose two devices (pump splitter and signal coupler) with different lengths in a single structure with no disruption to the pump or signal input fields. Two cases must be considered when dealing with different lengths.

Case 1: $L_p > L_s$

In this case the length of the pump splitter is greater than that of the signal combiner. That is $L_p = L_s + \Delta L$. To make this device possible, the multimode

section for the pump waveguide must be longer than that for the splitter waveguide. By tapering the end part of the pump waveguide, it can be assumed that the multimode section for the pump channel starts right at the beginning of the tapering, since the field pattern at the beginning of the multimode waveguide has a naturally tapered shape. The slope of the taper should be large enough, so that the field does not interact with the walls of the taper.

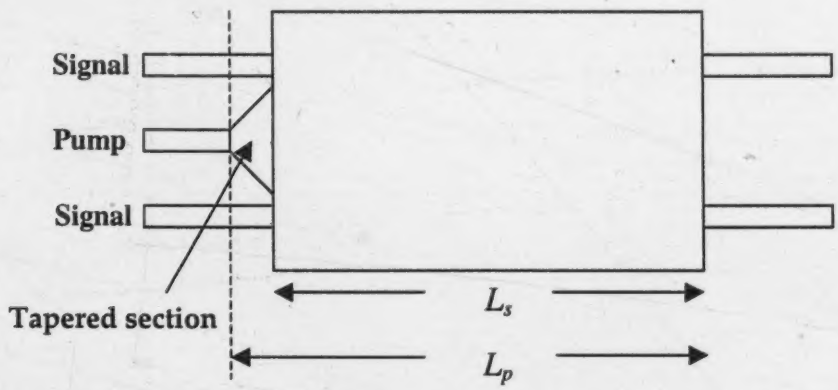


Figure 2.16 – Proposed structure (1) when $L_p > L_s$

Case 2: $L_p < L_s$

In this case the length of the pump splitter is smaller than that of the signal combiner. That is $L_s = L_p + \Delta L$. The signal channel input waveguides are tapered at the end which allows the actual length of the multimode section to be the sum of the taper length and the multimode waveguide length.

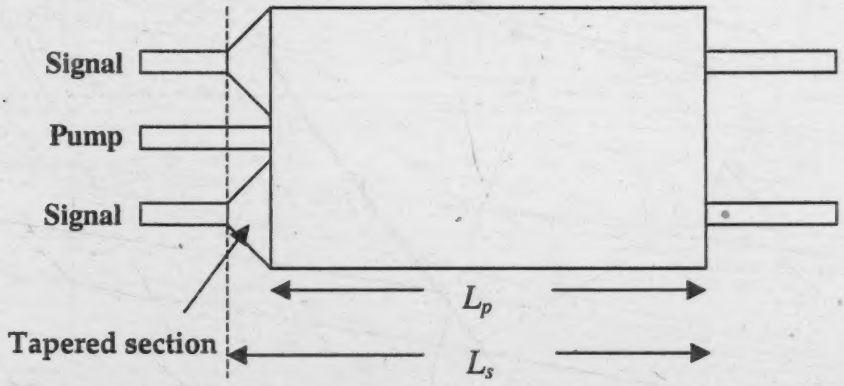


Figure 2.17 – Proposed structure (2) when $L_p > L_s$

The structure shown in Figure 2.18 can also provide the required length difference between the splitter and the coupler. However, with this structure the length difference that can be allowed will be smaller than that obtained with a taper for a constant separation between the pump and splitter access waveguides.

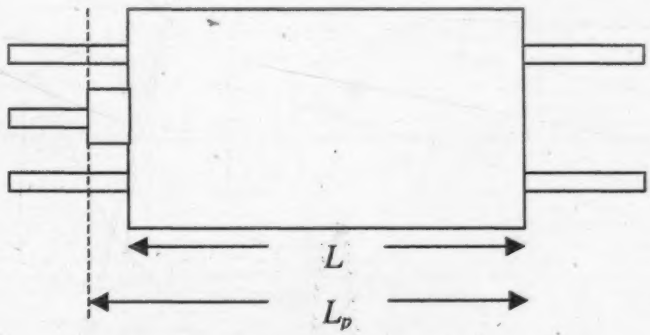


Figure 2.18 – Proposed structure (3)

However, there is a limit on the maximum value of $\Delta L$. Using ray optics a mathematical expression is derived in terms of the separation between the pump and coupler access waveguides of the multimode section and the refractive indices of the core and cladding as follows.

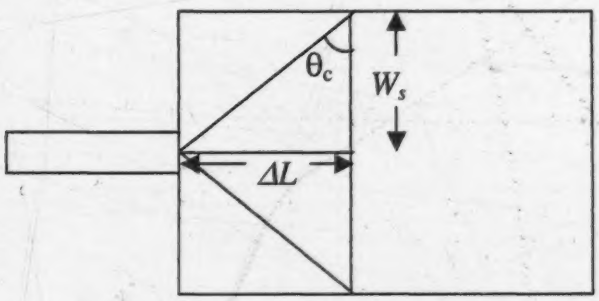


Figure 2.19 – Maximum limit on the $\Delta L$

Consider the critical angle (Section 2.1),

$$\sin\theta_c = \frac{n_{cle}}{n_{ce}}. \qquad (2.35)$$

From Figure 2.19,

$$\tan(\theta_c) = \frac{\Delta L}{W_s}, \tag{2.36}$$

where $W_s$ is the separation between the pump and signal access waveguides. Substituting Equation 2.35 in Equation 2.36 gives,

$$\Delta L \leq \frac{(W_s/2)n_{cle}}{\sqrt{n_{ce}^2 - n_{cle}^2}}. \tag{2.37}$$

Equation 2.37 gives an upper limit on the length difference. Increasing the separation between the access waveguides allows a larger length difference with the obvious tradeoff being a larger device. The parameters such as access waveguide separation, placement of access waveguides and index contrast should be optimized to design a low loss and small device.

### 2.6.2. Separation between access waveguides

The separation between access waveguides determines the width of the multimode section and hence the length of the device. Though close placement of access waveguides ensures smaller device dimensions, the crosstalk between two signal access waveguides sets a lower limit on the separation. However, the separation between the pump and signal access waveguides needs to be considered as it will be half of the signal waveguides separation.

The crosstalk is defined as

$$crosstalk = -10\log\left(\frac{P_1}{P_2}\right) dB, \tag{2.38}$$

where $P_1$ is the input power in one waveguide and $P_2$ is the power transferred to an adjacent waveguide. The power transferred from one waveguide to another can be calculated using the power coupling equation [43]

$$P_2 = P_1 \sin^2(KZ) \tag{2.39}$$

where $K$ is the coupling coefficient, and $Z$ is the length of the coupling region. The coupling coefficient between two symmetric slab waveguides is given by

$$K = \frac{2q^2 pe^{-ps}}{\beta t\left(q^2 + p^2\right)}, \tag{2.40}$$

where $q=\left[(n_c k_0)^2-\beta^2\right]^{\frac{1}{2}}$, $p=\left[\beta^2-(n_{cl}k_0)^2\right]^{\frac{1}{2}}$, $t$ is the thickness of the waveguide, $s$ is the separation between the waveguides, and $\beta$ is the fundamental mode propagation constant inside the waveguide. Crosstalk between two signal channels in the input waveguides results in noise in the output images. Similarly crosstalk between the pump and signal channels gives rise to a lossy device and the crosstalk between output waveguides gives noise in different signal channels.

### 2.6.3. Placement of access waveguides

Once the separation between the access waveguides is decided, their placement on the multimode section needs to be determined. Access waveguides are placed depending on the interference mechanism that is used. In this device, the placement must be compatible with both the splitter and coupler configurations.

First, the signal channel input waveguides placement is considered. When $N=2$, general or paired interference can be employed. However, for $N>2$, using restricted interference for imaging is completely ruled out, since restricted interference (both symmetric and paired) requires that the signal input waveguides are placed at $y=\pm\frac{W}{6}$ *or* $0$. Thus depending on the number of signals, imaging is possible by general or paired interference and the input waveguides are placed according to Figure 2.12 or 2.13.

The pump splitter input waveguide should be placed such that the pump power is uniformly split among the images. For a restricted interference splitter inputs placed at the center of the multimode section and at $\pm\frac{W}{6}$ only, yield uniform power splitting. Smaller device dimensions and small value of $\Delta L$ are the decision factors in selecting either paired or the symmetric interference.

Next, the placement of output waveguides should be considered. Placing the output waveguides at appropriate positions results in smooth coupling of the images into output waveguides and avoids any reflections [44]. The lateral positioning of the output access waveguides depends on the position of the images formed. Figures 2.11,

2.12 and 2.13 show the positions of the images and hence the positions of the output waveguides.

## Chapter 3 – 6X6 Pump-Signal Combiner: Modeling and Performance

The technique explained in Section 2.6 is applied to design a 6X6 pump-signal combiner. This combiner can feed 6 amplifiers simultaneously from a single pump source. The present chapter describes the actual device design and the difficulties in optimizing the dimensions. Some simulation results are also presented. The actual device design is started by selecting the material system. Section 3.1 explores the possible choices.

### 3.1. Material system

Of late, many new materials are being characterized for optical applications. Some of the key materials that are used in telecom applications are polymers, silica-on-silicon, silicon oxynitride ($SiO_xN_y$), lithium niobate ($LiNbO_3$), sol-gels, and silicon on insulator (SOI) [45].

Silica-on-silicon is a widely used planar waveguide technology. This material system has been used to realize lasers [46], amplifiers [47], couplers [48], filters [49], switches [50] and attenuators [51]. Silica waveguides show very low propagation (0.1 dB/cm) and coupling (1 dB) losses [52]. The main disadvantages in using silica waveguides are high stress in the core layers and polarization dependent losses.

$SiO_xN_y$ is gaining attention lately due to its core index tunability [53] from 1.45 ($SiO_2$) to 2.00 (SiON) and its excellent optical properties such as low losses at visible and near infrared light. The SiON layer is deposited using low-pressure CVD or plasma enhanced CVD requiring turn around times of the order of days, which makes these wafers expensive [54]. This material has been used to realize polarization controllers [55], filters [56] and attenuators [57].

SOI is being explored as a tentative alternative for the silica-on-silicon material system [58]. Unlike silica waveguides, silicon waveguides do not have any stress induced in the core layers. Literature shows that both active and passive devices have been fabricated in SOI. Passive devices such as multimode interference couplers [59], integrated 3 dB couplers [60], MXN star couplers [61], DWDM arrayed waveguide grating [62] and active devices such as photodetectors [63], [64] based on SOI have

been realized. Taking into account the high index contrast, low losses and ease of fabrication, the device described in this work is designed for a SOI rib waveguide material system.

### 3.2. Silicon on insulator

SOI consists of a $SiO_2$ layer sandwiched between the silicon device layer and the silicon substrate layer. Figure 3.1 shows an SOI rib waveguide.

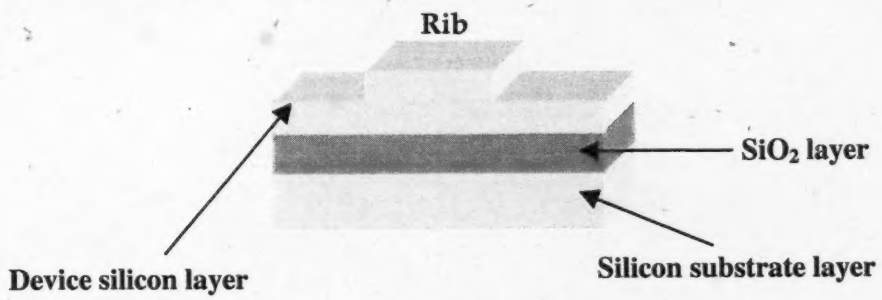


Figure 3.1 – SOI rib waveguide

There are three main methods of fabricating SOI substrates [65]:

1. Separation by implanted oxygen method (SIMOX): In this method a silicon wafer is implanted with oxygen at high doses ($10^{18}/cm^2$) followed by a high temperature annealing. As a result a buried oxide layer will be formed in the silicon wafer.
2. Bond and etch back method (BESOI): A silicon wafer is oxidized using wet or dry oxidation techniques followed by hydrophilic bonding to a bare silicon wafer and a subsequent heat treatment. The first wafer is then polished to desired thickness. However, the polishing might result in non-uniformity in the device layer.
3. Smart cut process: In this process an oxidized silicon wafer is implanted with hydrogen followed by a hydrophilic bonding to a bare silicon wafer. The wafer then undergoes a heat treatment. During the heating process the implanted wafer splits into two parts. One part will have a thin layer of silicon and the other one

has a buried oxide attached. This process provides a smoother surface than that obtained by BESOI.

Some of the advantages of SOI are:

1. High refractive index contrast

   SOI offers a very high index contrast due to the large index difference between silicon (3.5) and silicon dioxide (1.5) at 1550 nm. High refractive index contrast between the core and cladding allows tightly confining waveguides, which in turn helps in having smaller device features. Smaller devices are desirable in photonic integrated circuits for space reduction (or size).

   Multimode devices require high index contrast between the core and the cladding to have small phase errors. In addition, the access waveguides can be placed close together resulting in extremely compact devices.

2. Well-known fabrication techniques

   Silicon has been used, as the main substrate for integrated electronic chips for many years. It is comparatively well-characterized material and the waveguide fabrication methods are very well established.

3. Weak polarization dependence

   Polarization dependence in any waveguide is primarily due to the intrinsic material birefringence, stress in the core layer and the waveguide cross sectional asymmetry. The major cause for polarization dependence in silicon waveguides is the waveguide asymmetrical geometry. However, by tailoring the dimensions of the rib, the waveguide can be made polarization insensitive.

The silicon substrate that is used for modeling and fabrication has a 1.5 μm device silicon layer and 0.5 μm buried oxide layer. Table 3.1 shows the refractive indices of Si and $SiO_2$ at 1.55 μm and 1.48 μm.

| Material | Wavelength (μm) | Refractive index |
|---|---|---|
| Si | 1.55 | 3.477 |
| Si | 1.48 | 3.484 |
| $SiO_2$ | 1.55 | 1.527 |
| $SiO_2$ | 1.48 | 1.529 |

Table 3.1 – Refractive indices

### 3.3. Access waveguides

#### 3.3.1. Singlemode waveguide

Generally, access waveguides for a multimode interference device are single-moded. The access waveguides of the device in this project are also designed such that they guide only the fundamental mode. Consider a rib waveguide as shown in the Figure 3.2.

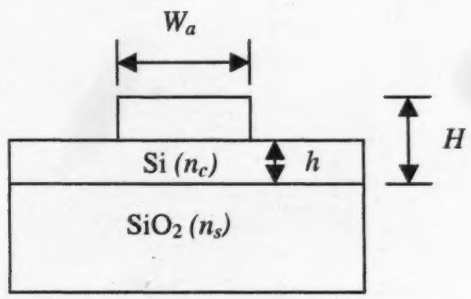


Figure 3.2 – SOI rib waveguide

Following the Marcatili's analysis (Section 2.4) on slab-coupled waveguides, the condition for singlemode (Equation 2.14) was plotted. The curves shown in the Figure 3.3 represent the smallest possible ratios $h/W_a$ and $h/H$ for singlemode propagation. These curves separate the region of singlemode operation and multimode operation. Dimensions of the singlemode waveguide were selected to be $h = 0.7\ \mu m$, and $W_a = 1.8\ \mu m$, which lie in the singlemode-operating region.

Using a commercial mode solver [66], the field pattern inside the rib waveguide was simulated and shown in Figure 3.4. It can be observed that the field is well confined inside the rib section of the waveguide. The field pattern inside the waveguide at 1.55

μm is not very different from the one at 1.48 μm and hence only the field at 1.48 μm is shown. Using the effective index method (Section 2.3.2.) the vertical fundamental effective indices of the waveguide were determined and are shown in Table 3.2. The effective indices were employed in running the 2D-BPM simulations, which shows the light propagation inside the waveguide (Figure 3.5).

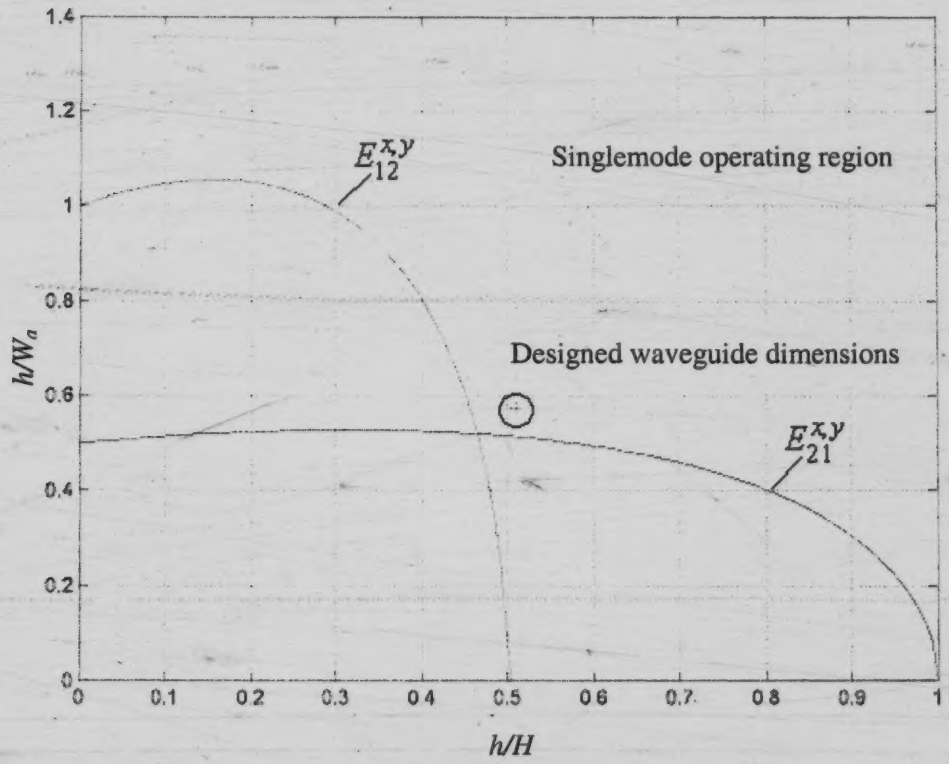


Figure 3.3 – Cutoff condition for higher order modes

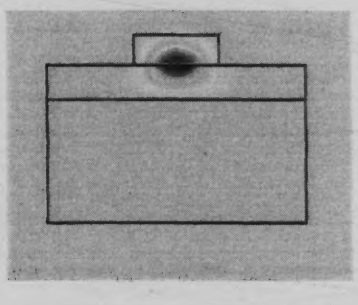

Figure 3.4 – Field pattern inside the rib waveguide at 1.48 μm

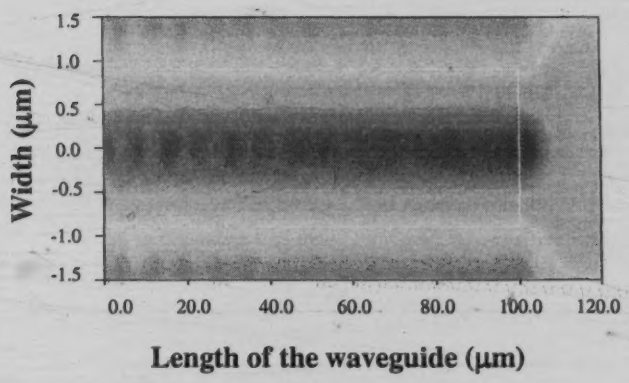


Figure 3.5 – BPM simulation of the light propagating inside the waveguide at 1.48 μm

| Material | Wavelength (μm) | Refractive index |
|---|---|---|
| Core | 1.55 | 3.4453 |
| Core | 1.48 | 3.4523 |
| Cladding | 1.55 | 3.3568 |
| Cladding | 1.48 | 3.3640 |

Table 3.2 – Fundamental effective indices of the rib waveguide

### 3.3.2. Separation between access waveguides

The minimum separation between two access waveguides was determined such that there is no significant crosstalk (< -25 dB) between them as explained in Section 2.6.2. Equation 2.40 was used in calculating the coupling coefficients for varying separating distances and shown in Table 3.3. Though the crosstalk between signal and pump channels will not result in noise in the output, it should be considered in order to reduce the insertion losses of the device.

| Waveguide separation (μm) | Coupling coefficient ($cm^{-1}$) |
|---|---|
| 2.0 | 375.1931 |
| 2.5 | 104.4197 |
| 3.0 | 29.0610 |
| 3.5 | 8.0879 |
| 4.0 | 2.2509 |
| 4.5 | 0.6265 |
| 5.0 | 0.1743 |

Table 3.3 – Coupling coefficients for varying separation between two waveguides

Crosstalk with varying separation between two waveguides of 100 μm is shown in Figure 3.6. Crosstalk at 100 μm was calculated since the access waveguides were fanned out to a separation of 125 μm after straight sections of 100 μm long.

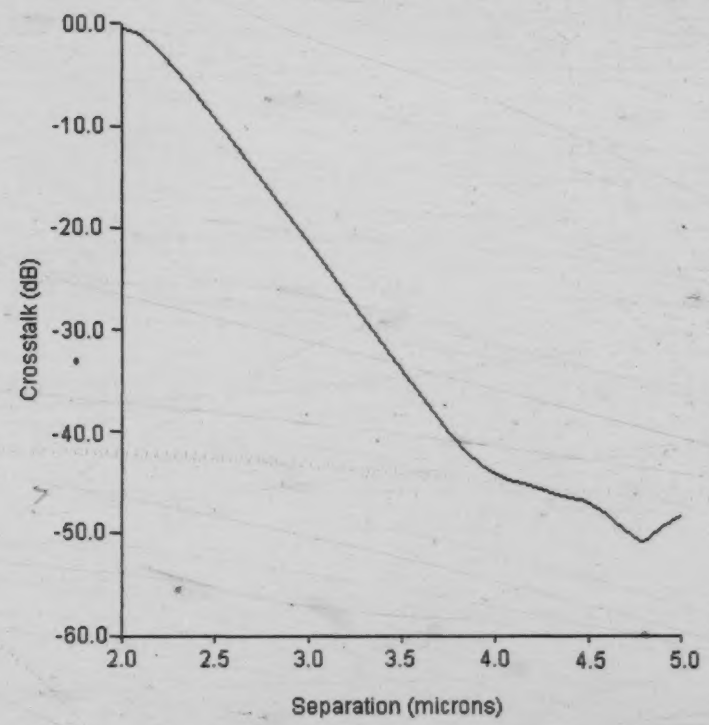


Figure 3.6 – Crosstalk between 100 μm long input waveguides

However, the plot shown in Figure 3.6 is valid for two straight (signal) waveguides only. This cannot be considered for the crosstalk between pump and signal waveguides due to the length difference tapering. Another plot has been drawn for the crosstalk with varying separation between the pump and signal channels (Figure 3.7) for the same waveguide length but with the taper in the structure. A waveguide separation of 4 μm gives a crosstalk less than –25 dB.

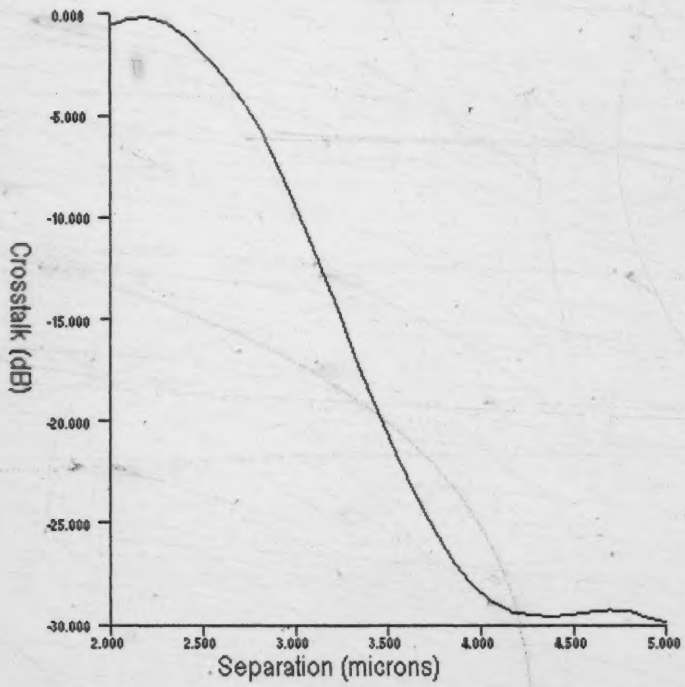


Figure 3.7 – Crosstalk between the pump and signal waveguides.

### 3.4. Calculating approximate width of the multimode section

After the access waveguide width (1.8 μm) and the separation between two access waveguides (4 μm) were determined, the approximate minimum width of the multimode section was calculated. Consider the output port for the paired interference splitter configuration (Figure 2.13) with an access waveguide separation of 4 μm. Then,

$$2\frac{W}{3N} = 4\ \mu m \tag{3.1}$$

For a 1x6 splitter ($N$=6) the width is 36 μm. The length of splitter and coupler were calculated to be 11922 μm and 11781 μm respectively at $p = 17$ and listed in Table 3.4.

| | Beat length (μm) | Length (μm) |
|---|---|---|
| Splitter | 4159.4 | 11781 |
| Coupler | 3974 | 11922 |

Table 3.4 – Calculated lengths of the splitter and coupler for a paired interference device

Similarly, the width of the multimode section was calculated from the symmetric interference configuration at the output port (Figure 2.14). In this case, $\frac{W}{N} = 4$ μm for which the width is 24 μm. However, at the input section, on both sides of the pump channel, signal channels are to be fed at the positions where the splitter forms images. The separation between pump and the signal channels has to be greater than or equal to 4 μm (Section 3.3.2). When the width of the multimode waveguide is 24 μm, 3 access waveguides need to be placed in a width of 4 μm, which is not feasible. Hence, instead of taking the output waveguide separation as a reference, input waveguide separation is considered.

Referring to Figure 2.13,

$$\frac{W}{6} = 8\ \mu m \tag{3.2}$$

from which $W$ is 48 μm. Coupler length was calculated to be 21016 μm and length of the splitter is 21093 μm at $p = 17$. Table 3.5 shows the calculated lengths of the splitter and the coupler.

| | Beat length (μm) | Length (μm) |
|---|---|---|
| Splitter | 7337.05 | 21093 |
| Coupler | 7005.6 | 21016.8 |

Table 3.5 – Calculated lengths of the splitter and coupler for paired interference device

In theory, the splitter based on paired interference provides smaller dimensions than that of the one based on symmetric interference. However, the theoretical length difference with symmetric interference is much larger than it is with paired interference compared to the allowed length difference of approximately 10 μm (Equation 2.37).

Though the length difference is small, the actual dimensions of the device are large compared to many other passive devices on an integrated circuit. Thus, length reduction possibilities were explored. Equation 2.26 shows that the length of the device is proportional to the square of the width. In an attempt to reduce the length, the width of the device was decreased. It was observed that a micron reduction in the separation of the pump and its adjacent signal waveguide results in a change of width from 48 μm to 36 μm. However, this increases the insertion loss of the signal channel due to the reduction in separating distance with the pump waveguide. In order to avoid this, S-bends were introduced at the signal inputs adjacent to the pump channel, which can provide 1 μm offset. The Figure 3.8 shows the light propagation inside the S-bend. The radius of curvature of the S-bend was optimized to have losses as low as 0.3 dB/cm.

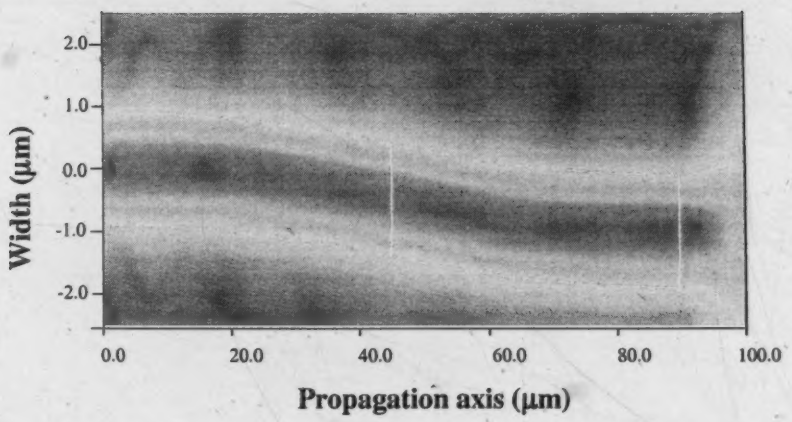


Figure 3.8 – Light propagation inside an S- bend

### 3.5. Length calculations for the splitter and the coupler

The length of the device with the changed width was calculated again. The length at which single image formed was found to be 11922 μm (Equation 2.26) for the signal wavelength. The splitter length at which six images formed was calculated to be 11957.7 μm (for p = 30) and the length difference is 35.7 μm. By introducing the S-bends a length reduction of approximately 43% was achieved.

Figure 3.9 shows the final structure of the device. Since the length of the splitter is larger, the pump channel waveguide was tapered at the input of the multimode section. The output access waveguides were also tapered in the final design. This serves two purposes. Firstly, tapering reduces the reflections[44], and secondly, it couples light efficiently into the output waveguides. The access waveguides were actually separated at 4 μm for about 100 μm from the multimode section. Using S-bends the access waveguides were fanned out at a 125 μm pitch. This is necessary for testing the fabricated device and conforms to the standard diameter of optical fiber.

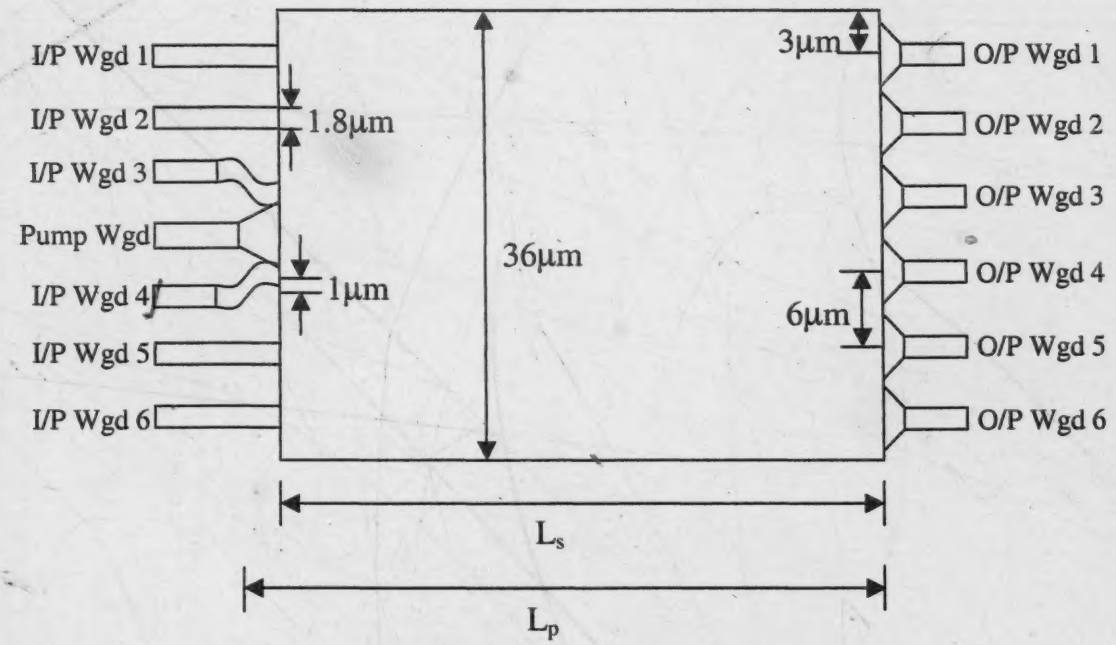


Figure 3.9 – Proposed structure for 6x6 multiplexer

### 3.6. Simulation results

The propagation constant $\beta_m$ given by Equation 2.23 is an approximation. Due to this, the phases accumulated by the modes will deviate from the calculated values and results in blurring of the images. Blurring of the images can be avoided by slightly adjusting the calculated dimensions. Using BPM simulations, the device dimensions were optimized.

The optimization process for low losses was complicated by the fact that both the splitter and coupler performance must be taken into consideration. The main parameters that were optimized for low insertion losses in the simulations were the length of the multimode section and the length of the tapering.

The length of the multimode section was adjusted such that the splitter and coupler offer low losses and low crosstalk. Plots were drawn with varying length against the insertion loss in both the splitter and coupler. The insertion loss is defined as

$$loss = -10\log\left(\frac{P_o}{P_i}\right) \quad dB \tag{3.3}$$

where $P_o$ is the output power and $P_i$ is the input power.

Figure 3.10 shows the coupler insertion loss sensitivity as a function of length. Coupler insertion loss for signal inputs at waveguides 1, 2 and 3 are shown in the picture. The signal input through the waveguide 3 shows more losses compared to the other two for the same length. This is due to the fact that the waveguide 3 and the pump waveguide were placed close together near the multimode section.

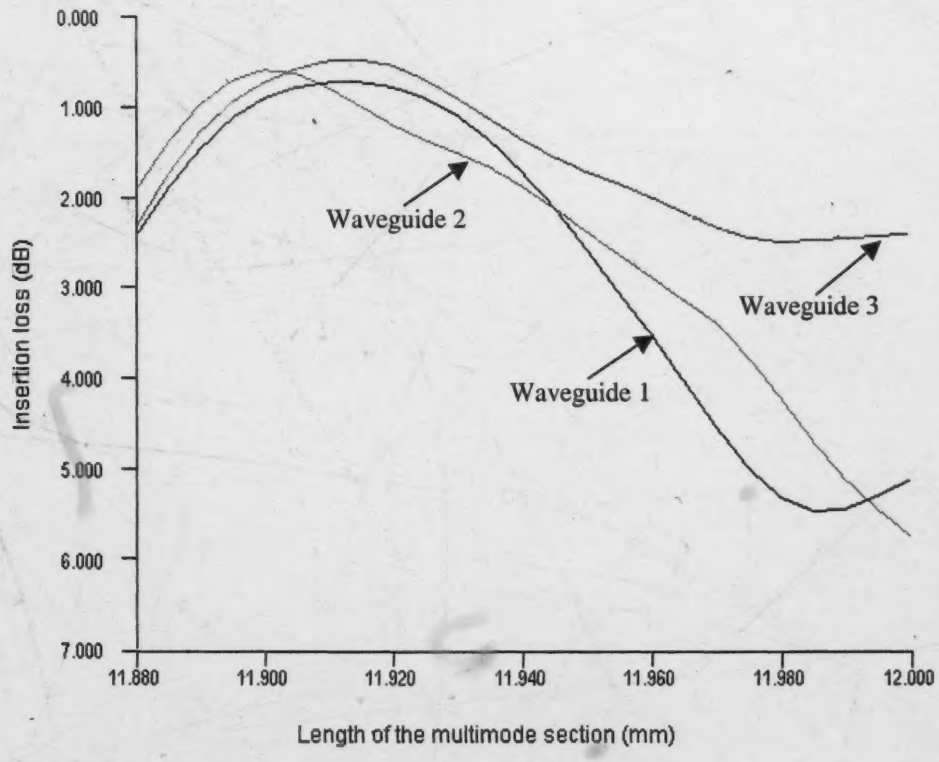


Figure 3.10 – Insertion loss sensitivity to the length

Although the S-bends are placed between the pump and signal channel, the 1 μm offset provided by it is gradual and there is coupling of signal channel into the pump taper. Thus, the multimode section effectively starts earlier for waveguide 3, than for waveguides 1 and 2. This explains the shift in the optimal length for the waveguide 3. To support this argument, simulations were run for the signal coupler waveguide without the pump waveguide in the structure (to eliminate the effect of the input

tapering) and a 0.5 dB reduction in insertion loss at an optimal length of 11922 μm was observed.

While considering the coupler performance, it was required to consider the crosstalk. Here, the crosstalk represents the unwanted power in any other output waveguides except for the one that is supposed to receive all the power. For example, the input in waveguide 1 should form an image at output 6 and, ideally all the power should be transferred to the same waveguide. However, some power will be collected by the adjacent waveguide 5 and comparatively lower powers will be collected by the remaining waveguides. If the power input to waveguide 1 is $P_o$ and power collected in waveguide 5 is $P_i$, the crosstalk in dB is defined as

$$crosstalk = -10\log\left(\frac{P_o}{P_i}\right) \quad dB. \tag{3.4}$$

Figure 3.11 shows the variation of crosstalk (Between the input waveguide 3 and output waveguide 5) with varying length. As the length is moved away from the optimal value crosstalk increases.

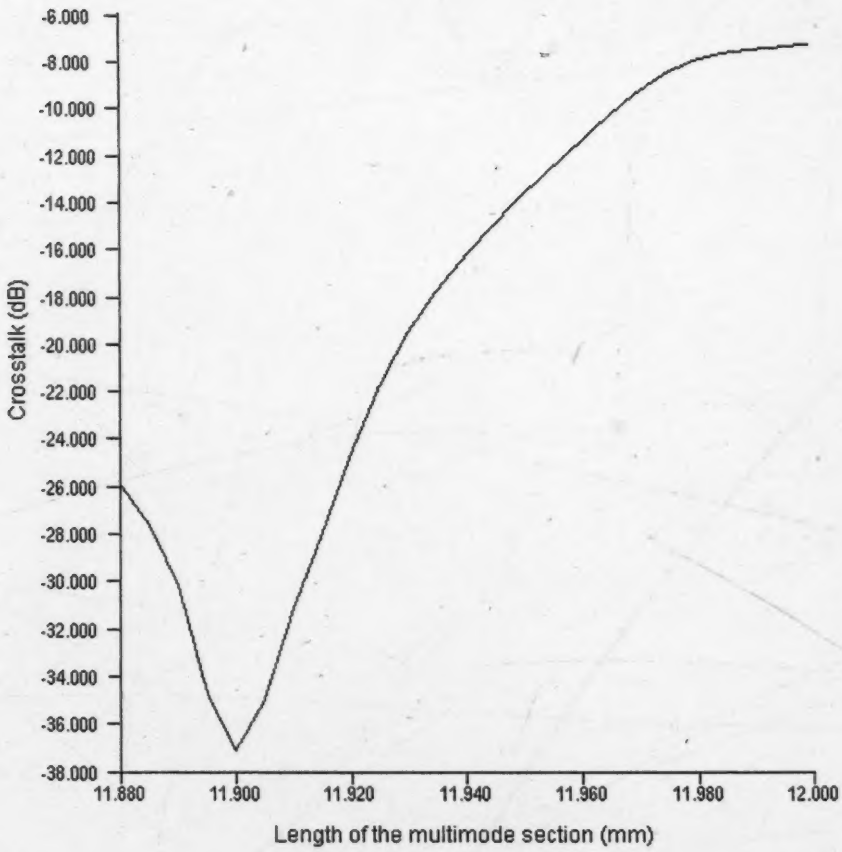


Figure 3.11 – Crosstalk

Figure 3.12 shows the variation of splitter insertion loss with length. Due to the symmetry of the field distribution in the images formed at waveguides 1 and 6, waveguides 2 and 5, and waveguides 3 and 4, the insertion losses observed in these pairs closely match. In the range of optimal lengths, the power splitting is well balanced, but away from the optimal values the power split is not equal among all the images resulting in an imbalance. To choose an optimal splitter length, the imbalance was also taken into consideration.

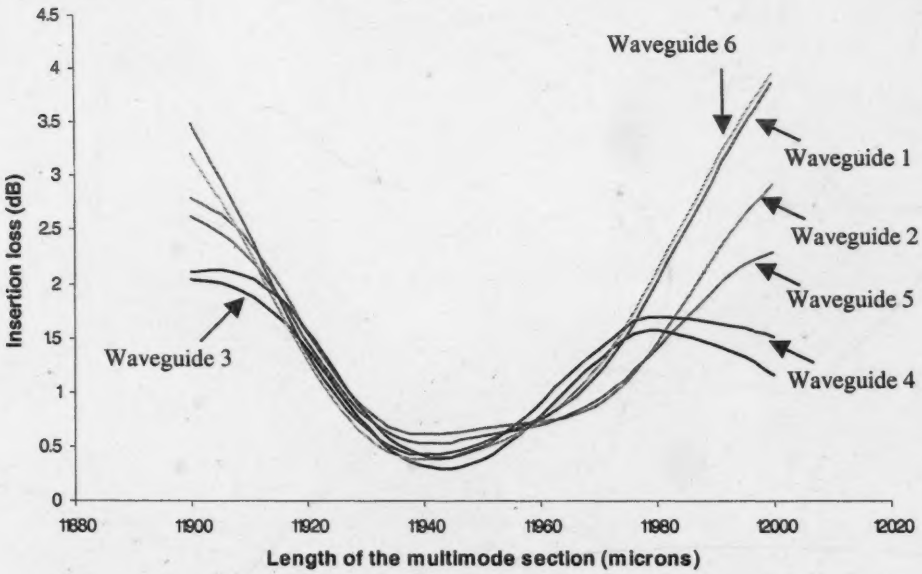


Figure 3.12 – Sensitivity of insertion loss to the splitter length

The taper length was also varied to see how the coupler and splitter losses would change. The optimal taper length was found to be 38 μm. An increase of 10 μm in the taper length decreased the splitter losses by 0.3 dB. However, the same increment in taper length increased the coupler losses by 0.52 dB. The loss was increased only in the coupler at waveguide 3. Other couplers at waveguide 1 and 2 have shown no significant change in the losses, since the increment in taper length starts to disrupt only the input field in waveguide 3.

To decide on the optimal length of the device both the splitter and coupler performances were considered. At an optimal length of 11922 μm and a taper length of 38 μm, the coupler losses and splitter losses were calculated and shown in the Table 3.6a and 3.6b. The splitter insertion losses were higher than the coupler insertion loss. It is because of the fact that the designed taper length is 38 μm and the maximum allowed using Equation 2.37 is only 10 μm.

| Waveguide number | Insertion loss (dB) |
|---|---|
| 1 | 0.771 |
| 2 | 0.759 |
| 3 | 0.759 |
| 4 | 0.759 |
| 5 | 0.759 |
| 6 | 0.771 |

Table 3.6a – Splitter insertion losses

| Waveguide number | Insertion loss (dB) |
|---|---|
| 1 | 0.4 |
| 2 | 0.39 |
| 3 | 0.93 |

Table 3.6b – Coupler insertion losses

The intensity pattern of the field inside the optimized device obtained by BPM simulations is shown in Figures 3.13a and 3.14a. The start and end fields are also shown in the pictures Figures 3.13b and 3.14b. The coupler output field shows that not all the power is in the image of the input field but some of it is lost in the form of signal noise. It is also observed that the output field is slightly wider than the input field. Splitter output field shows an even distribution of power among all the images. The energy conservation was checked and the total output energy is within 98.4% of the input energy.

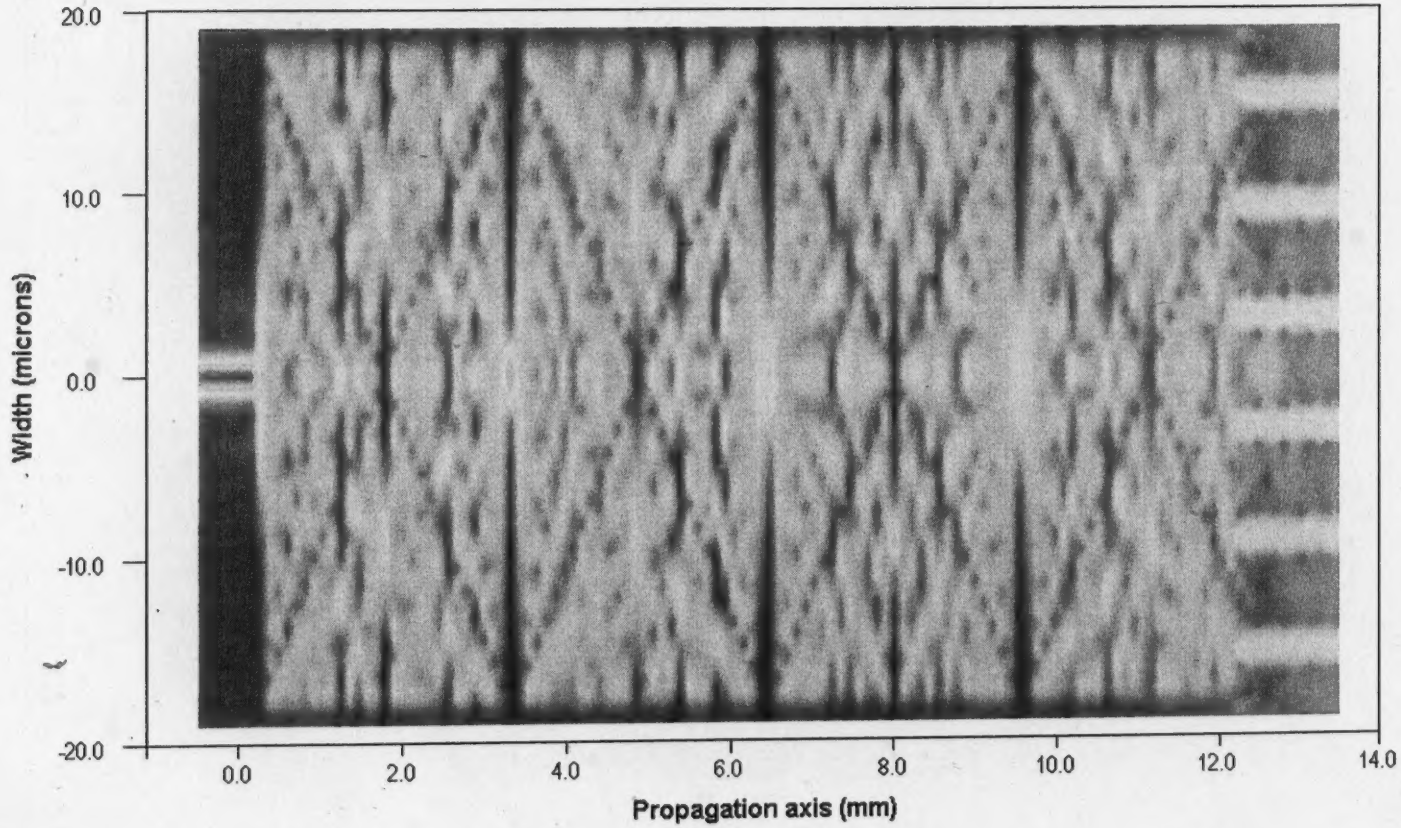


Figure 3.13a – BPM simulation of the splitter

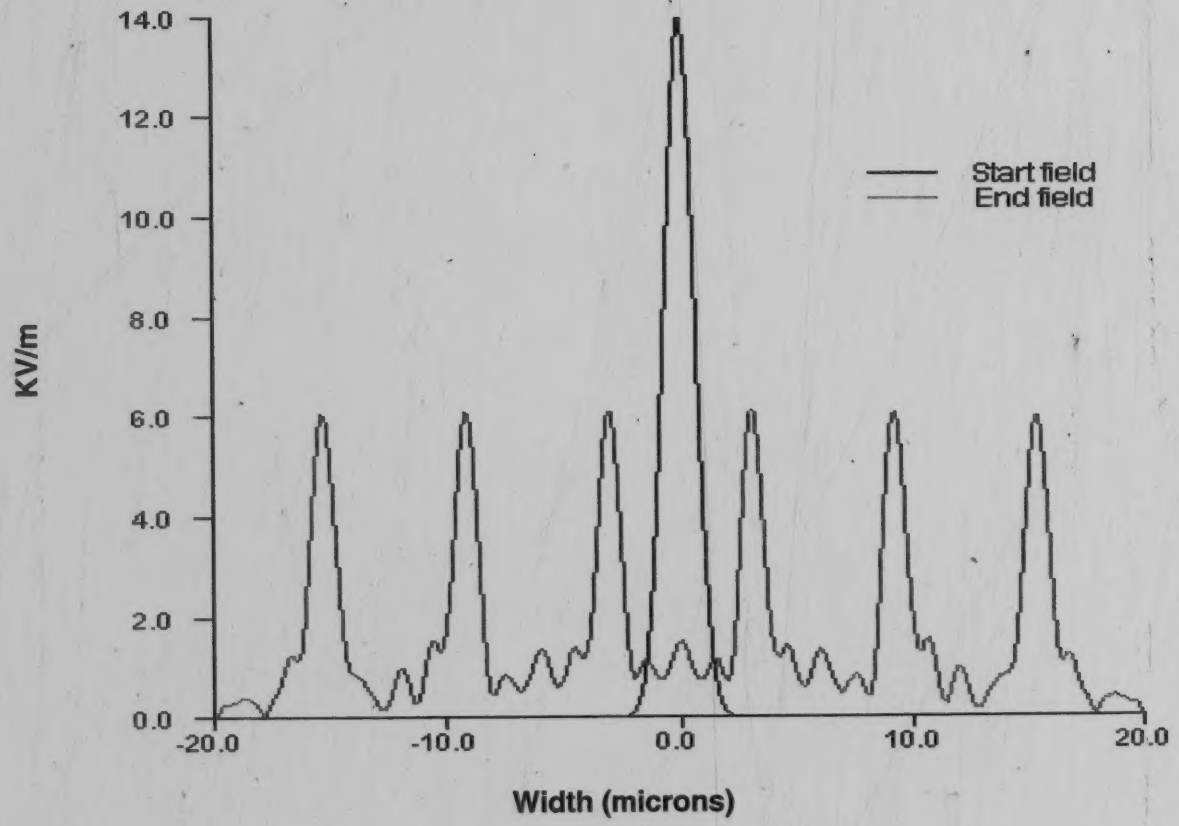


Figure 3.13b – Start and end fields of the splitter

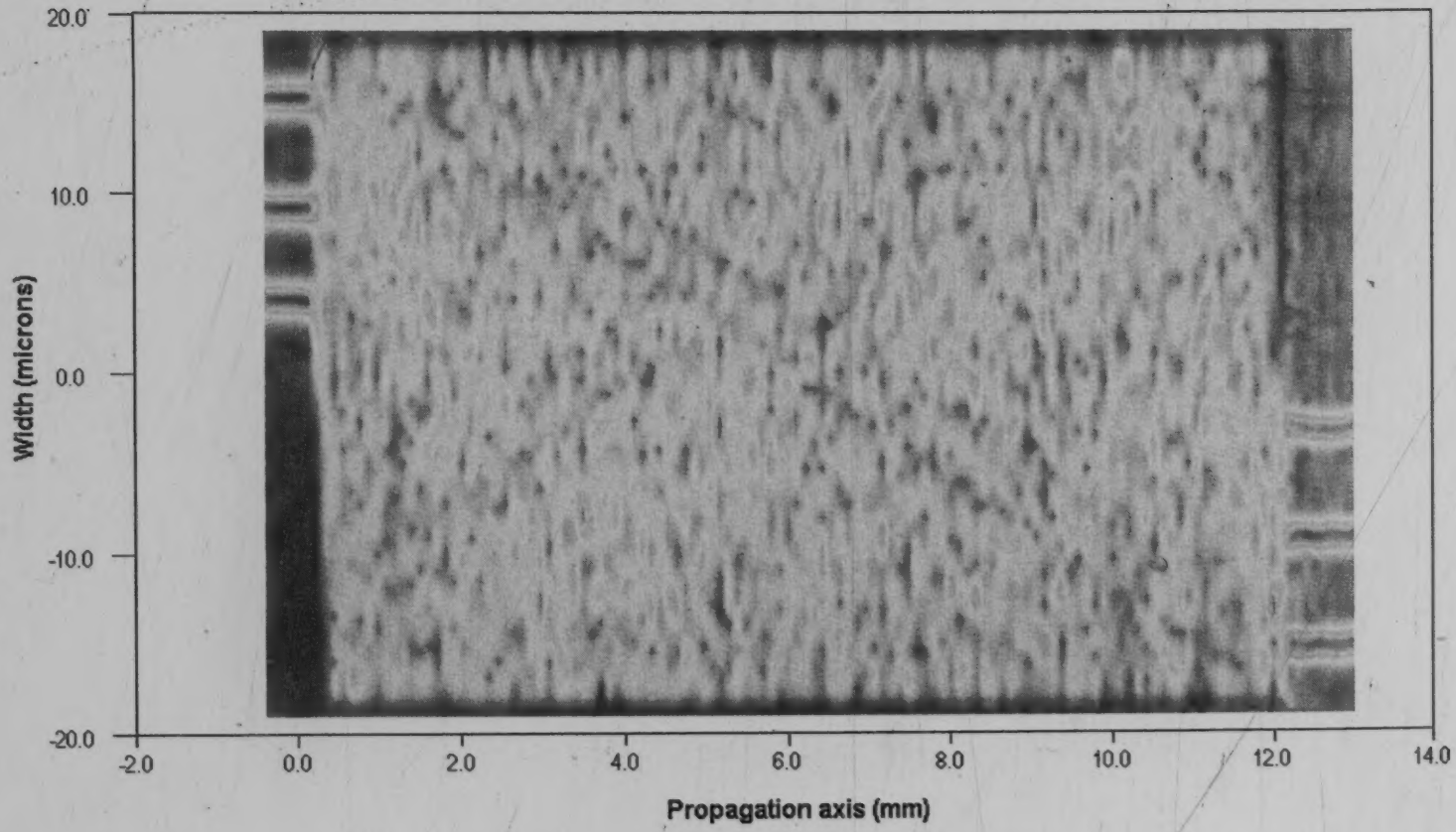


Figure 3.14a – BPM simulation of the coupler

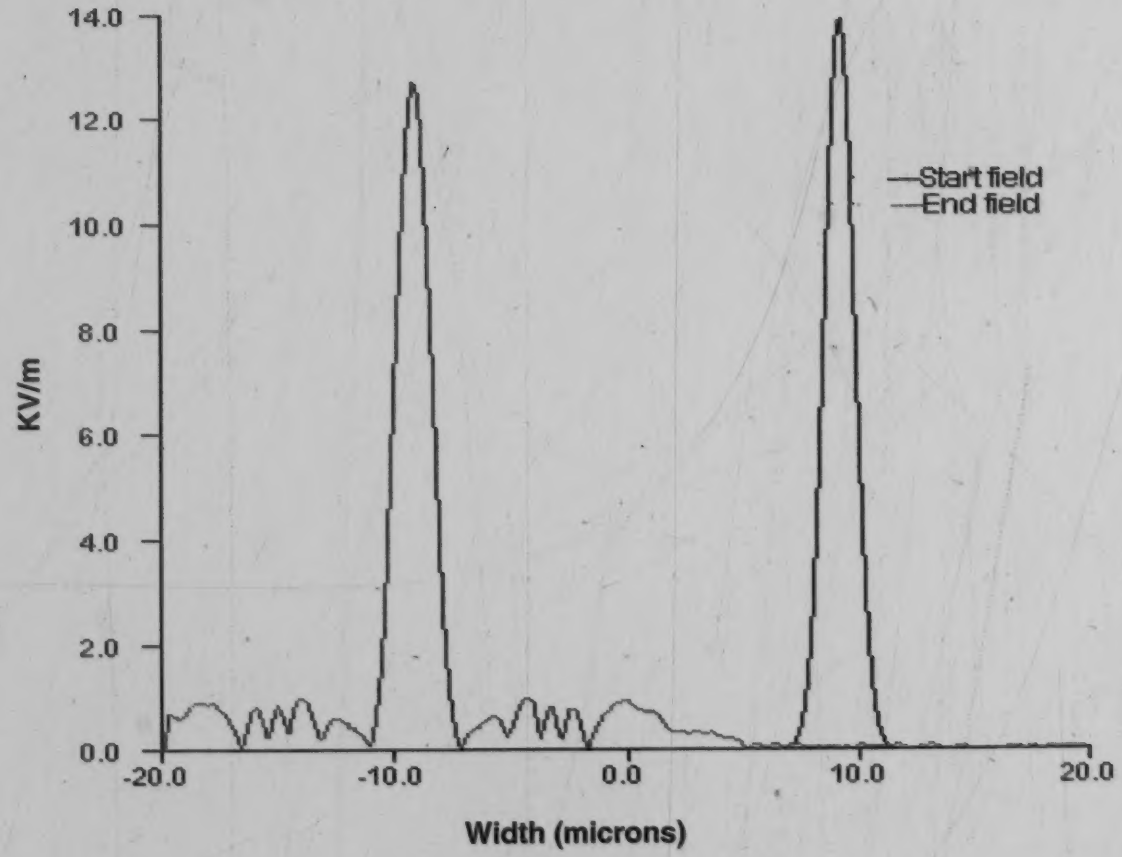


Figure 3.14b– Field pattern of the splitter

The field pattern of the splitter has been checked to confirm the conservation of energy.

The sensitivity of the coupler insertion losses to the width variation was also explored. A plot was drawn with varying width and insertion losses (Figure 3.15). It can be observed that the losses are very sensitive to the width variation. A variation of $\pm 0.5W\%$ in width increases the losses by 3 dB. This is because the length of the multimode waveguide varies as the square of width. More relaxed fabrication tolerances were observed for the length variation. A 3 dB increase in the losses was observed for a tolerance of +/- 40 μm from the optimal length (Figure 3.10).

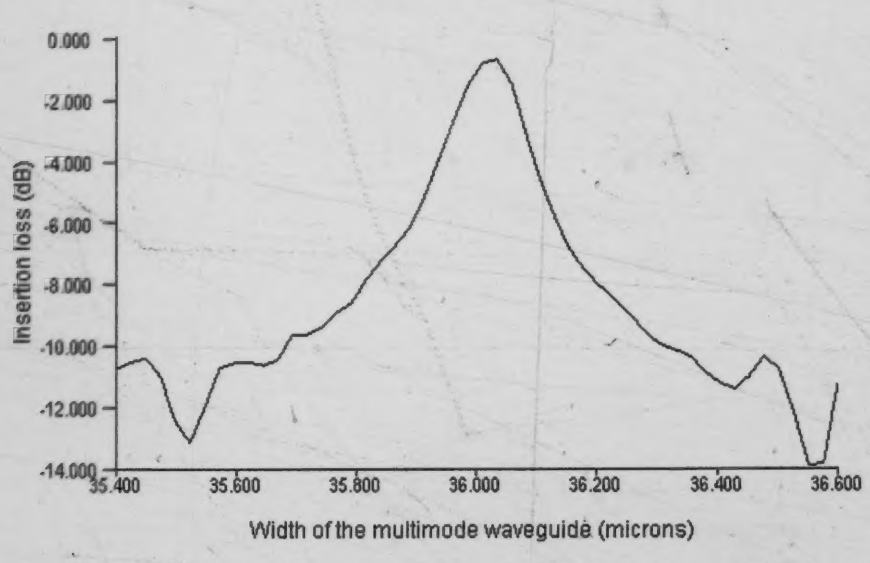


Figure 3.15 – Sensitivity of insertion loss to the width variation

The device showed a wavelength tolerance of +/- 4 nm from the central wavelength. For an approximate variation of +/- 3 nm in the central wavelength, a 3 dB increment in loss was observed (Figure 3.16). The wavelength tolerance for the 6X6 multiplexer is relatively small compared to the 2X2 multiplexer reported in Ref. 21. This is because the number of channels in the device designed in this thesis is larger and higher the number of channels, lower the optical bandwidth [67]. However, this smaller bandwidth was not expected to pose any difficulty for an efficient performance of the device, as 8 ITU channels with 0.8 nm spacing can be placed in 7 nm.

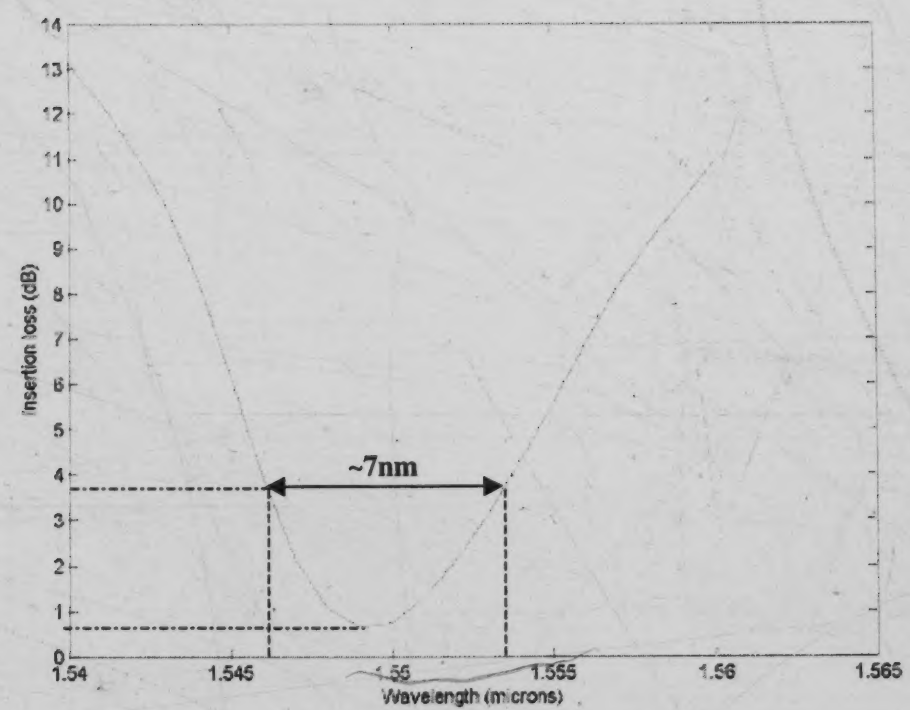


Figure 3.16 – Coupler performance against varying wavelength

# Chapter 4 – Device Fabrication

This chapter describes the fabrication procedure of the MMI device designed in Chapter 3. Fabrication procedures for silicon waveguides are well standardized [68] and these methods were followed in this project. The following sections describe the entire process and the difficulties in achieving the waveguide anisotropy and smooth sidewalls.

The main steps involved in the fabrication process are

1. Mask designing
2. Wafer cleaning
3. Resist spinning
4. Exposing the wafer to UV radiation
5. Developing the photoresist
6. Etching the wafer

## 4.1. Mask design

A mask is essentially a stencil used to transfer the device layout onto the wafer. Masks are made of quartz or optically flat glass with the device pattern on them, usually defined in chrome or aluminum. When the UV light is shone on the mask, the quartz and the glass are transparent to it and the light passes through, but the chrome pattern blocks the UV radiation from passing through.

A prototype mask (Figure 4.1) was designed using Alcatel OlympIOs mask design software and the mask was manufactured by a commercial supplier [69]. The mask has an anti-reflection chrome pattern on it, written by e-beam lithography. 100 devices were written on the mask with various dimensions. The dimensions were varied to compensate for the errors that might occur during fabrication. The length of the multimode section was varied from 11915 μm to 11930 μm, and the width was varied from 35.5 μm to 36.5 μm. The features on the mask have a critical dimension tolerance of 0.1 μm. This critical dimensional tolerance of the mask is not expected to affect the critical dimensions of the device as the device dimensions were varied on the mask

layout. Vertical and horizontal dicing marks were also placed on the mask for convenient dicing of the wafer into small samples.

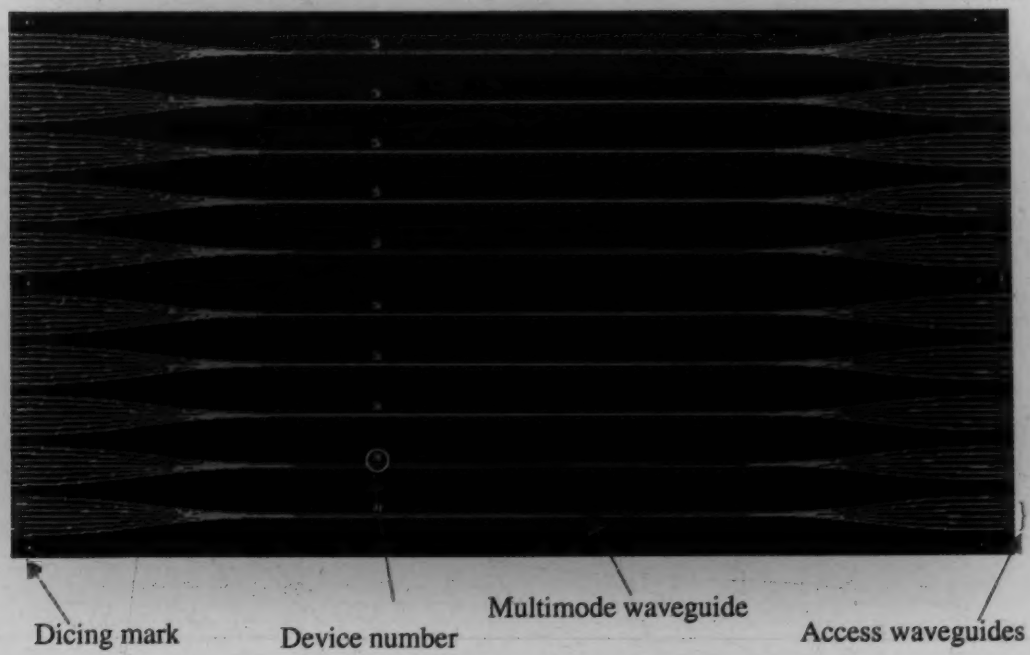


Figure 4.1 – Prototype mask

**4.2. Photoresist**

UV sensitive chemical properties of a photoresist make it an essential material to be used in photolithography. A photoresist consists of three main components, a polymer, a sensitizer and a casting solvent. The solvent helps in spinning and forming thin layers, the polymer changes its structural properties with UV illumination and the sensitizer controls the process. When the photoresist is exposed to the UV light, the polymer chains are weakened or broken resulting in a change in their solubility in developing solutions.

There are two kinds of photoresist, positive and negative. Solubility of a positive photoresist increases by approximately ten times and that of a negative resist reduces by ten times when exposed to UV. For the device fabrication, a positive photoresist was used as it can transfer the pattern efficiently with a minimum feature size of 0.5 μm.

Usually, photoresist is spun on the wafer using a resist spinner. Uniformity in resist thickness is a major factor determining the accuracy of the pattern transfer. If the amount of resist that formed the layer is more than the required, ridges or hillocks are

formed. Too little resist may not cover the entire wafer. Both are detrimental to accurate pattern transfer. Hence the speed of the spinner needs to be optimized to avoid these problems.

Before the actual fabrication was started, the wafer needed to be cleaned to get an efficient pattern transfer [70]. The wafer was cleaned with a standard piranha solution consisting of 3 parts of $H_2SO_4$ and 1 part of $H_2O_2$. Substrate was placed in the solution for 15 minutes, which removed organic impurities and metallic contaminants from the wafer surface. After cleaning with piranha, the substrate was rinsed with distilled water. The wafer was then baked at 120°C for 30 minutes to remove any water molecules that were present after cleaning.

After the wafer was cleaned and dried, a standard adhesion material HMDS was spread on the wafer to enhance the adhesion of photoresist to the wafer strongly. A standard positive photoresist (SPR – 504) was spun at 4000 rpm for 45 seconds to form a layer of 1.4 μm. After spin coating, the wafer was soft baked at 75°C for 10 minutes to avoid any built-in stress. Soft baking also helps in improving the adhesion of the resist layer to the silicon.

### 4.3. Exposing to UV

The soft baked wafer was then transferred to a UV exposing system (ABM Mask aligner "ELMO" in the U of A Nanofab facility). The mask was aligned with the wafer and the UV rays were passed on to the wafer through the mask for 4 seconds. This radiation produces a chemical reaction in the exposed photoresist, which results in a change of solubility. In the next step the wafer was developed in a standard developing solution (Developer – 354) for 22 seconds. After developing, the wafer was checked under the microscope to confirm a good pattern transfer. The middle portion of the input section of the multimode waveguide could not be transferred on to the wafer accurately. If the wafer was left in the solution for longer than 25 seconds, the waveguides were broken. Developing for less time resulted in the photoresist not being completely removed. This may be due to the fact that the waveguides are closely spaced. An optimum developing time of 23 seconds was set, such that there were no broken waveguides.

### 4.4. Etching

Etching is the final process involved in fabricating the device. It is the pattern transfer by chemical or physical removal of the material from the substrate in a pattern defined by the protecting mask layer. There are two main types of etching, wet etching and dry etching. In selecting an etch process, the etch profile as a function of depth has to be considered. The designed rib waveguides require smooth and vertical walls, and good critical dimensional (CD) control for the efficient operation of the device. Hence the etching process should yield anisotropic sidewalls and accurate pattern transfer.

Anisotropy is attainable with both the dry and wet etching techniques [71],[72],[73]. However, anisotropic wet etching often leaves a rough surface, which increases the scattering loss of the device [68]. Also wet etching techniques do not offer a good control over CD. In dry etching, the anisotropy and surface smoothness can be controlled by the plasma conditions. Hence dry etching was chosen for the device fabrication.

Reactive ion etching (RIE) or plasma etching is the standard dry etching process employed in fabricating silicon devices. A plasma etching system consists of an etching chamber, vacuum pump, gas supplies and an RF power source. The schematic of an RIE machine is shown in Figure 4.2. Initially the vacuum chamber is pumped down to a low pressure (~100 mTorr). A reactive gas (halocarbon gases like $CCl_4$, $C_2F_8$ or $SF_6$) is allowed into the reacting chamber and a radio frequency signal is passed through. The RF signal breaks up the gas molecules and creates plasma of reactive chemical species capable of reacting with the silicon layer. These ions may physically remove the Si layer or they may chemically react with the silicon depending on the pressure inside the chamber.

When the pressure inside the chamber is less than 100 mTorr, the actual material removal is done physically. The material is ejected by the bombardment of highly energized ions. When the pressure inside the chamber is of the order of 100 mTorr, both physical and chemical processes are included in etching. If the pressure is higher than 100 mTorr, etching is due to chemical reactions between the process gases and the silicon.

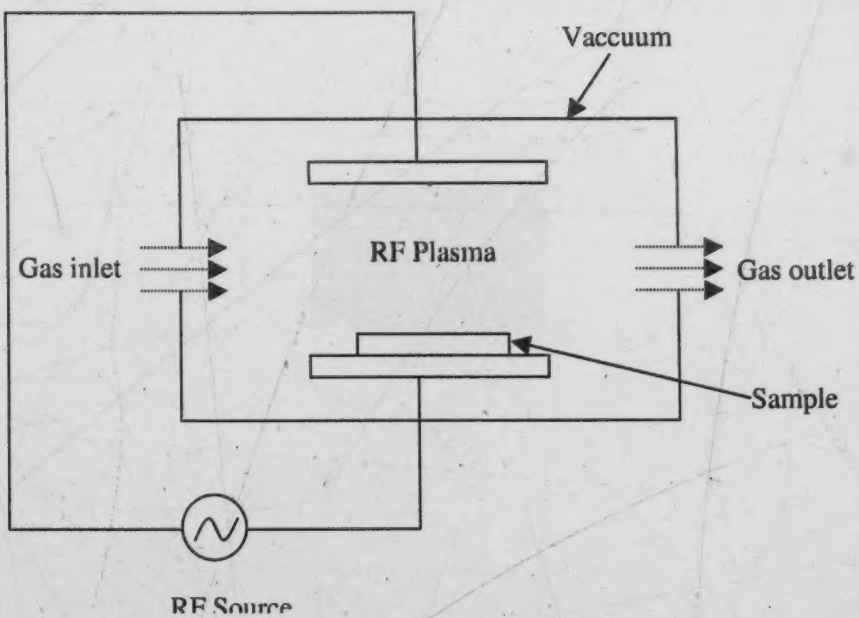


Figure 4.2 – Schematic of reactive ion etching

Etch recipes vary from system to system [74], [75] and the parameters need to be optimized separately for each system. Several runs were performed with various parameters such as $SF_6$ flow rate, pressure inside the chamber and the duration of etching. An optimum set of values was decided upon for the required 0.8 μm etch and shown in the Table 4.1. Since the etch depth is only 0.8 μm the photoresist itself was used as the etch mask.

| | |
|---|---|
| $SF_6$ flow rate (sccm) | 26 |
| Initial chamber pressure (mTorr) | 100.56 |
| Power (watts) | 50 |
| Etch rate (μm/min) | 1.06 |

Table 4.1 – Silicon etching recipe

Using the recipe shown in the Table 4.1 the etched waveguides were found to be isotropic (Figure 4.3) and the sidewalls of the waveguide (Figure 4.4) have a roughness

of about 100 nm. The isotropy in dry etching process can be avoided by adjusting the plasma conditions. Reducing the pressure inside the chamber will actually increase the anisotropy [68], but the selectivity of the etching between the photoresist etch mask and silicon is reduced. As a result the photoresist mask might be etched away along with the silicon. When the pressure is too low, the etching is purely physical and high-energy ions sputter away the silicon layer by bombarding the surface. However, if the energy of the ions is too high, the surface will be rough.

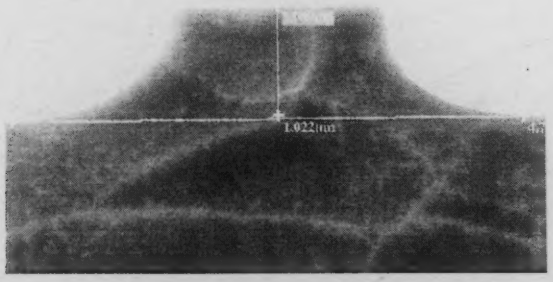

Figure 4.3 – Cross sectional view of a rib waveguide

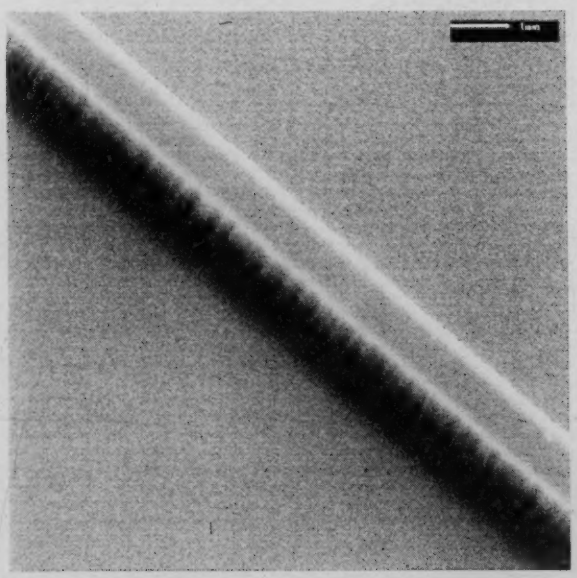

Figure 4.4 – Top view of a rib waveguide

It should be noted that the scale bar shown in the picture corresponds to a length of 1 μm.

### 4.5. Anisotropic silicon dry etching technique - Sidewall passivation

The most successful techniques of anisotropic etching are based on sidewall passivation [71],[72]. In this method, additional passivating gases such as oxygen, hydrogen, and $BCl_3$ are allowed into the etching chamber along with the usual etch gas. These gases react with the surface and form a protective layer, which prevents lateral etching.

The ion bombardment removes this passivating layer from the horizontal surface and etches it. This results in sidewall verticality for the rib waveguide. In the $SF_6/O_2$ chemistry, oxygen reacts with the silicon and a layer of silicon dioxide is formed on the horizontal surface as well as on the sidewalls of the rib waveguide. The fluorine radicals remove the oxide layer on the horizontal surface before they start etching, by forming volatile products. The oxide layer on the sidewalls is not removed, which will help in achieving the anisotropy.

The oxide layer on the sidewall will change the optical properties of the device, and it needs to be removed once the etch is completed. However, removal of the oxide layer actually changes the feature dimensions. Since the mask pattern has a number of devices with varying dimensions, it is expected that achieving critical dimensions should not be a problem. The addition of passivating gases into the chamber reduced the etch rate and the parameters for the process needed to be re-optimized. Table 4.2 shows the optimized process parameters.

| | |
|---|---|
| $SF_6$ (sccm) | 26 |
| Oxygen flow rate (sccm) | 5 |
| Initial chamber pressure (mTorr) | 100.56 |
| Power (watts) | 50 |
| Etch rate (μm/min) | 0.325 |

Table 4.2 – Silicon etching recipe with sidewall passivating gas

SEM pictures of the etched rib waveguides show that the etch is anisotropic (Figure 4.5) and the sidewalls are smooth. It has been observed that the etch depth was different for different waveguides, even though they were etched simultaneously. This is illustrated in Figure 4.6a and b. In Figure 4.6a, the silicon layer was etched to 0.815 μm, while waveguide shown in Figure 4.6b was etched down to 0.635 μm. The scale bar shown in the pictures corresponds to 100 nm.

Figure 4.5 – Cross sectional view of a rib waveguide

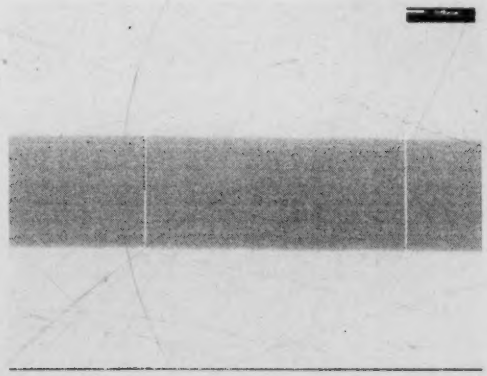

Figure 4.6a – Side view of rib waveguide

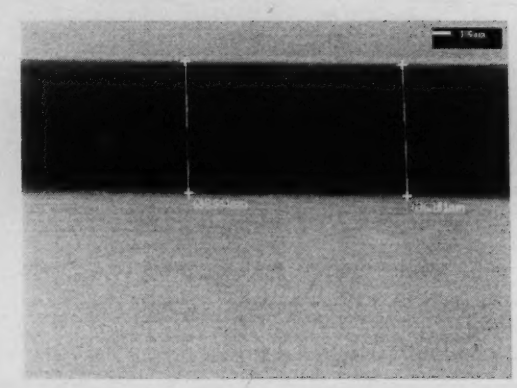

Figure 4.6b – Side view of rib waveguide

There are two possible reasons for this variation in the etch depth. The first is that the etch mask may not have protected the surface of the silicon uniformly. The second potential cause is non-uniformity in the silicon layer itself since the photoresist

mask was still remained on the wafer after etching. Using the profilometer the non-uniformity of the silicon layer was measured and a thickness variation of 0.5 μm was observed (Figure4.7).

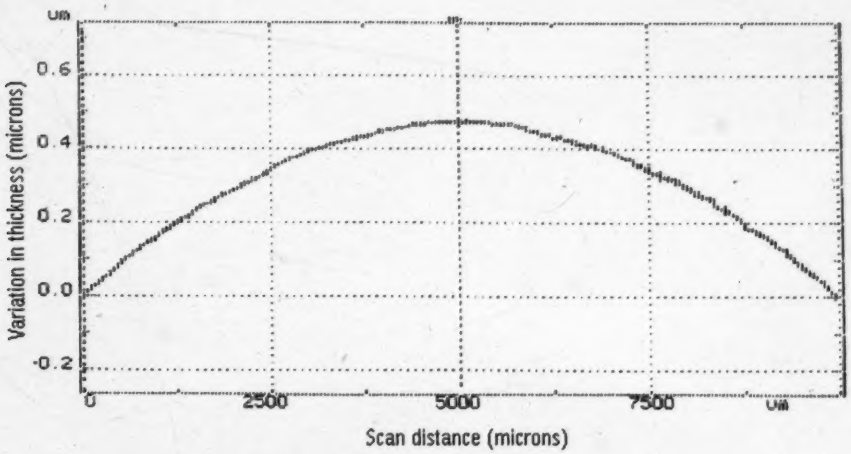


Figure 4.7 – Thickness variation in silicon layer

The output waveguides are very well defined as shown in Figure 4.8. The input section of the multimode waveguide was not defined in the fabrication as it was designed (Figure 4.9a). It should be noted that the scale bar on the picture represents 1 μm. The three waveguides at the center were supposed to be separated from each other but they are not separated for about 70 μm and the S-bends are not formed. It was observed that this change in device structure is due to a problem in the mask, microscope picture of which shown in Figure 4.9b confirms this. It is suspected that there was a problem in the translation of the layout to the mask file.

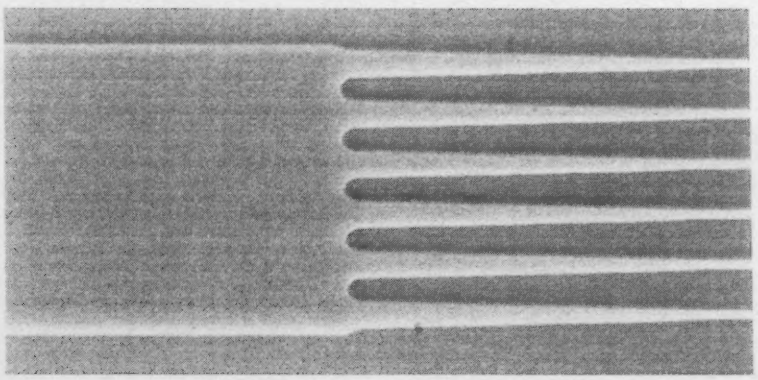

Figure 4.8 – Output section of the multimode waveguide

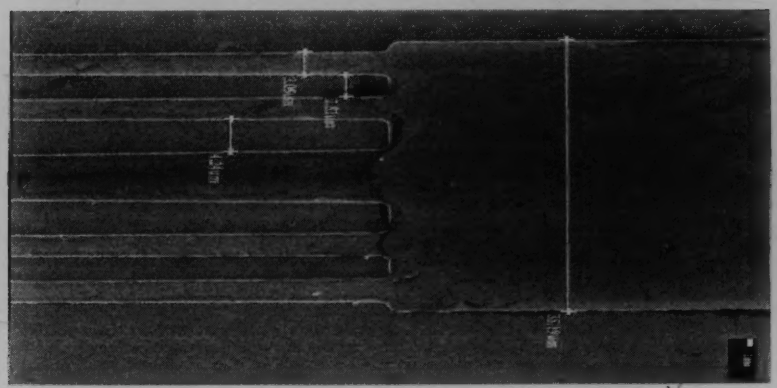

Figure 4.9a – Input section of multimode waveguide

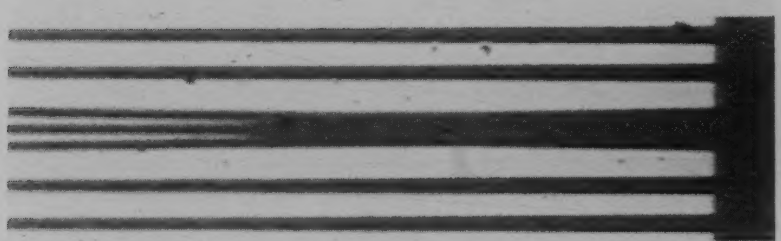

Figure 4.9b – Multimode section input layout on the mask

This change in the waveguide structure will not effect the operation of signal channels in waveguides 1,2,5 and 6. However, the pump performance is expected to degrade. Simulations were again run with the structure shown in Figure 4.9a. The splitter imbalance was increased to 1.61 dB with the maximum and minimum insertion losses being 0.41 dB and 2.02 dB.

Figures 4.10 and 4.11 show microscope pictures of a single sample at different positions. In Figure 4.10, the device silicon layer is evident even after etching. However, in Figure 4.11, no device silicon layer was observed on the sides of the rib. The reason for this is the silicon layer thickness variation. Another consequence of this non- uniformity in the thickness will be a variation in the effective refractive index of

the waveguide core along the length of the waveguide. This will prevent the image forming at the end of the multimode section since the beat lengths for the modes will not be the same as designed.

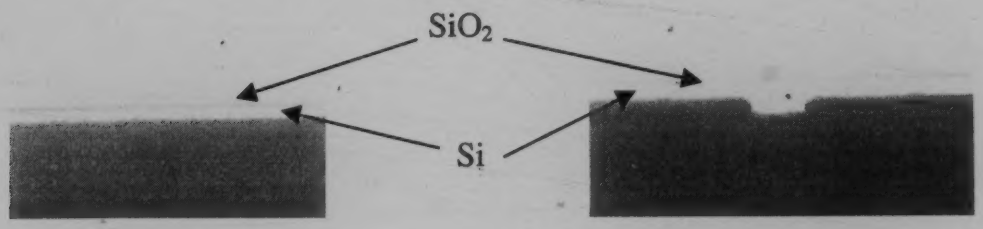


Figure 4.10a – Sample edge

Figure 4.10b – Rib waveguide

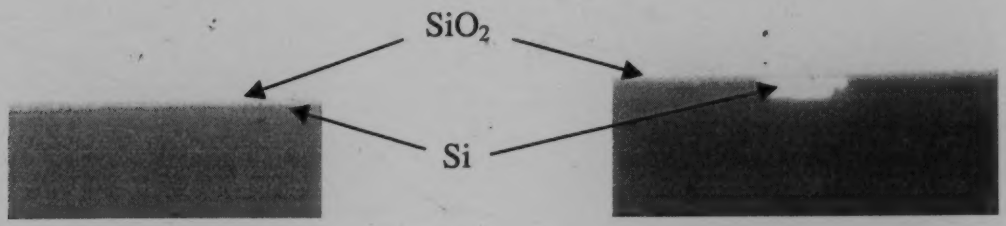


Figure 4.11a – Sample edge with no device silicon layer

Figure 4.11b – Silicon ridge waveguide

# Chapter 5 – Device Characterization

Waveguides and devices are usually characterized by measuring their transmission and coupling losses [76]. Due to the major difficulties in fabricating the device and the poor surface quality of the substrate, it was impossible to experimentally confirm the device performance. However, in this chapter device-testing method is explained.

Transmission losses include absorption loss, scattering loss and mode conversion loss and coupling losses constitute mode mismatch loss and Fresnel reflection loss. The loss measurement experiment gives the total losses of the device, where

$$\text{total losses} = \text{coupling losses} + \text{transmission losses.} \quad (5.1)$$

The coupling losses are calculated theoretically and the total losses are determined experimentally, from which the transmission losses are found.

## 5.1. Coupling losses

Coupling losses are the losses that occur during the light coupling from the fiber to the waveguide. The two main coupling losses, Fresnel reflection losses and mode mismatch losses are explained in the following sections.

### 5.1.1. Fresnel reflection losses

This loss is due to a step change in the refractive index of the propagation medium. When light is fed into the waveguide from a fiber, the light reflects at the fiber-air interface and the air-waveguide interface. Due to this, some light reflects back into the fiber as shown in Figure 5.1. The resulting losses are called, Fresnel reflection losses.

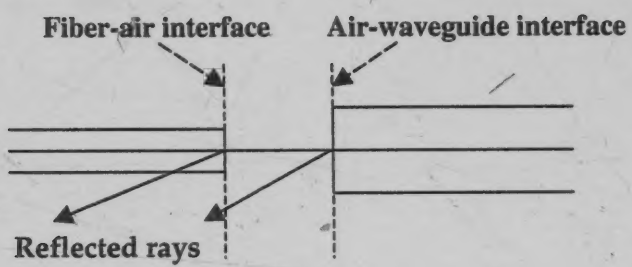


Figure 5.1 – Fresnel reflections

The Fresnel reflection coefficient $R$ which measures the fraction of the power reflected at each interface is given by

$$R = \left( \frac{n_1 - n_2}{n_1 + n_2} \right)^2, \tag{5.2}$$

where $n_1$ and $n_2$ are the refractive indices of the materials at the interface. At the air-fiber interface the reflection coefficient was calculated to be 0.04 and at the air-silicon waveguide interface it is 0.308. Losses at each interface in dB is given by

$$loss = -10\log(1-R) \quad dB. \tag{5.3}$$

These losses are on both input and output sides of the waveguide and the fiber end. Fresnel's reflection losses can be minimized by using an index matching gel or by using anti-reflections coatings.

### 5.1.2. Mode mismatch losses

A major portion of coupling losses between the input fiber and the waveguide are due to the modal mismatch between the fiber fundamental mode and the waveguide fundamental mode. The modal mismatch is measured in terms of coupling efficiency.

The coupling efficiency of a waveguide is calculated using a gaussian approximation for the fundamental mode in both the fiber and the waveguide [3]. The coupling efficiency is given by

$$\eta = 4 \frac{{d_f}^2 + {d_w}^2}{\left( {d_f}^2 + {d_w}^2 \right)^2}, \tag{5.3}$$

where $\eta$ is the coupling coefficient, $d_f$ and $d_w$ are the mode field diameters of the fundamental mode in the fiber and the waveguide, respectively.

Commonly, a tapered fiber or lens coupling is employed to reduce the modal mismatch between the fiber mode field and the waveguide mode field. In lens coupling a collimating lens and an objective lens are placed in between the fiber and the waveguide to reduce the spot size. Spot size reduction will help in achieving a low coupling loss if the fiber mode field diameter is larger than the waveguide mode field.

Modal mismatch losses increases by the mis-alignment between the fiber and the waveguide. The three basic coupling errors that occur during fiber alignment are longitudinal misalignment (Figure 5.2a), lateral misalignment (Figure 5.2b), and angular misalignment (Figure 5.2c).

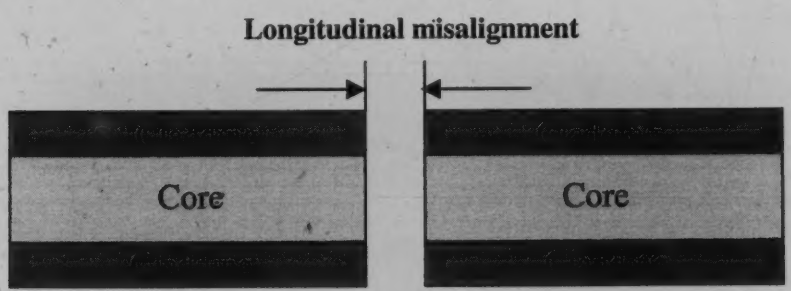


Figure 5.2a – Longitudinal misalignment

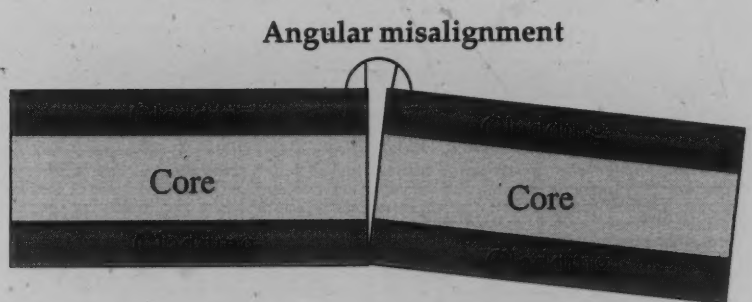


Figure 5.2b – Angular misalignment

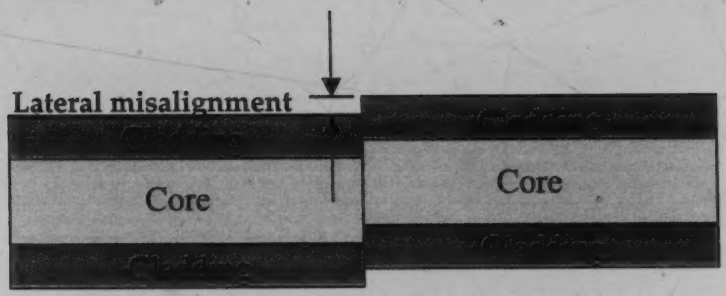


Figure 5.2c – Lateral misalignment

## 5.2. Scattering losses

The reasons for scattering losses in a waveguide are sidewall roughness, structural imperfections in the waveguide, imperfections in the core and cladding interface, and unclean core top surfaces [2]. Microscopic variations in material density will also cause scattering losses (Rayleigh scattering). Some of these losses can be avoided by having smooth sidewalls and no imperfections on the waveguides. However, the fabrication process did not yield perfectly smooth sidewalls. Hence, some scattering loss is expected at the sidewalls.

## 5.3. Preparing the sample

After fabrication, the wafer was diced into small samples (~2 cm x 1 cm). Dicing left the sample edges very rough (Figure 5.3a) and some of the waveguides did not extend to the end of the sample and were unusable in this state. These rough facets will also increase the scattering and coupling losses at the fiber and waveguide interface. The samples were polished with a 1 μm sample polisher followed by a 0.3 μm sample polisher to obtain smooth facets (Figure 5.3b). After polishing the sample, these samples were cleaned with distilled water and ethanol to remove any dust particles sticking to the sample.

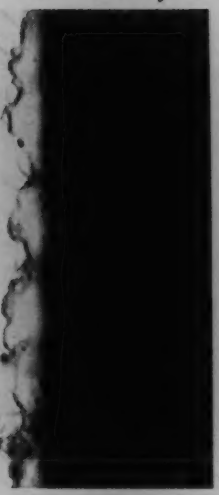

Figure 5.3a – Unpolished sample edge

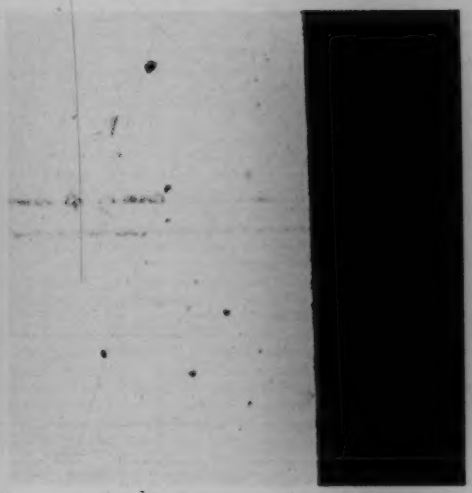

Figure 5.3b – Polished sample edge

### 5.4. Experimental setup

Since the device is supposed to work both as a pump splitter and a signal combiner, it needs to be tested at both 1480 nm and 1550 nm respectively. The same experimental set up as shown in Figure 5.4 was employed in testing the devices at the two wavelengths. Figure 5.5 shows the photograph of the experimental set up in which an objective lens was placed to capture the end view of the waveguide.

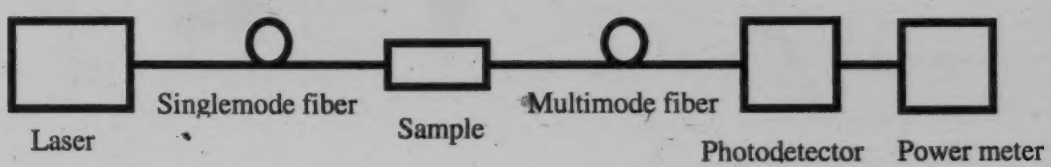


Figure 5.4 – Schematic of experimental set up to characterize the device

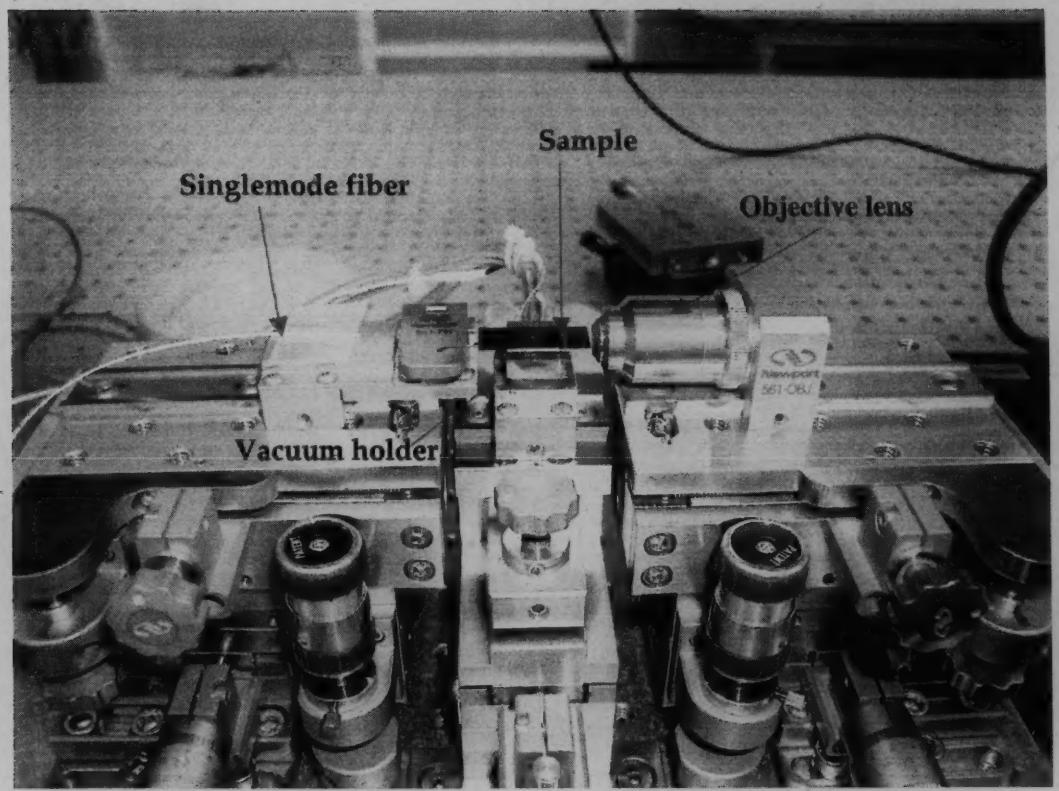


Figure 5.5 – Photograph of experimental set up to characterize the device

To test the device, a singlemode fiber was butt-coupled to the end of the sample and a multimode fiber was butt-coupled to the output of the sample to collect the light. Butt coupling is a very simple method used to excite modes in a waveguide in which the input fiber is placed very near to the waveguide. Sub-micron accuracy in aligning the fiber with the waveguide is required to minimize the mode misalignment losses. Small misalignments will excite higher order modes in the waveguide resulting in higher losses. The coupling station that was used for the experiment has micrometers capable of measuring 500 nm movements axially, 1 μm laterally and, 1 μm vertically. This helped in achieving a good alignment with the waveguide.

### 5.5. Difficulties in testing the device and possible solutions

The singlemode input fiber that was used in butt-coupling to the waveguide has a mode field diameter of 4.6 μm. From the simulations, the fundamental mode field

diameter in the waveguide is expected to have 3 μm. Using Equation 5.3, the coupling efficiency of the waveguide was calculated to be 20.9%. Hence, a coupling loss of 6.9 dB is expected on the input side. This is considered to be a very high coupling loss compared to 1 dB reported by Ref.52. The difference between the mode field diameters is the main reason for high coupling loss.

Coupling light into the access waveguide was a difficult task due to the small dimensions (3 μm x 0.8 μm) of the waveguide compared to the fiber dimensions. When the light was launched into the waveguide, it was coupled to the adjacent slab section along with the rib waveguide. This resulted in light entering the multimode section at arbitrary positions, which would increase the crosstalk.

An IR digital camera and a frame grabber were used to capture the top view of the light going through the waveguide and some fringes were observed on the sample (Figure 5.6). It was also observed that light is being scattered in a regular pattern along the length of the device. The reasons for light scattering can be change in the index profile, discontinuities in the device structure, dirt, or non-uniform waveguide thickness. Buried oxide etching (BOE) has been performed on the sample to find out if these fringes were formed due to any oxide deposition. However, it was observed that even after BOE the fringes could be seen. Which implies that there was no index change due to the formation of an oxide layer. The sample was tested under the microscope to check if there are any discontinuities in the structure. The device was observed to be continuous and no broken waveguide were found.

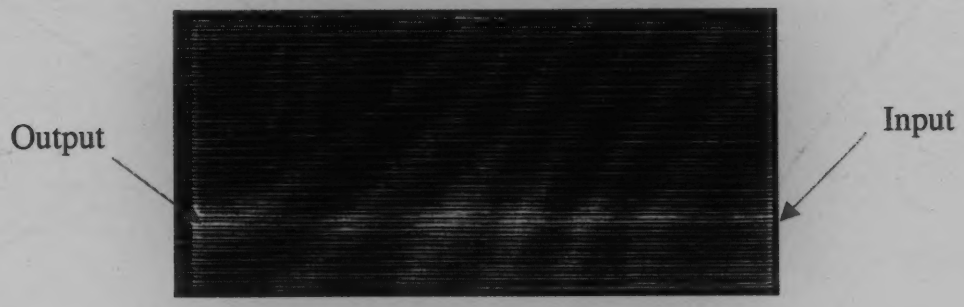


Figure 5.6 – Top view of light going through the sample

It is believed that the thickness variation in the silicon device layer (Figure 4.7) or surface roughness has given rise to the scattering. Bright spots were observed at the positions where the surface is rough and at the positions where the thickness is varied.

Figure 5.7 – Picture of a sample

A white light picture of the sample is shown in Figure 5.7. A portion of concentric rings can be observed. These dark and light rings may be interference patterns formed due to the silicon layer thickness variation. This is for the evidence of the non-uniformity of the guiding layer reported in Chapter 4.

## Chapter 6 – Conclusions

In this project, a pump/signal combiner that can feed six amplifiers simultaneously in an integrated optical amplifier module was designed and simulated. An attempt was made to fabricate the device on SOI material system. Since the device can simultaneously send light into multiple amplifiers using a single pump laser, the complexity, cost and the size of the integrated amplifier module may be reduced considerably.

In the device, a pump splitter was superimposed with a signal coupler. By exploiting the dead zones at the corners of the multimode waveguide, the splitter and combiner with different lengths were superimposed in a single structure. The entire design process involved optimization of different parameters such as effective refractive index of the core, width of the multimode section and length of the tapering (which compensates the length difference between the splitter and coupler). The main goal in optimizing these parameters was to minimize the length difference between the pump splitter and signal combiner and hence the losses of the device.

The combiner was designed for a SOI rib waveguide system. The properties of the SOI, such as low polarization losses and high index contrast, made it a suitable choice. Using slab coupled waveguide theory the dimensions of the singlemode access waveguide were determined. The access waveguide separation was also determined considering the crosstalk as the limiting parameter. The width of the multimode section was determined, such that all the access waveguides can be placed on it according to the image formation. The same procedure was repeated for different values of parameters until the length difference had an acceptable value. For the 6x6 multiplexer designed in this work, the simulated insertion losses are shown in the Table 3.6a and 3.6b.

The sensitivity of the device performance to the variation in width and length were determined. A variation of ±0.5% in width increases the losses by 3 dB. A 3 dB increment in loss was observed for +/-40 μm length tolerances. The bandwidth of the device was found to be 8 nm, which can accommodate approximately 10 DWDM channels with 0.8 nm channel spacing.

An attempt was made to fabricate the device using standard silicon device fabrication techniques. Using photolithography, the device pattern on the mask was transferred onto the SOI wafer. Reactive ion etching was employed to etch the rib waveguide structure. Anisotropy of the rib was the main problem faced in fabrication. Using sidewall passivation techniques, the anisotropy was reduced considerably. However, due to the problem in mask designing software, device could not be fabricated as designed. This may be avoided by increasing the spacing between the waveguides.

## 6.1. Suggested future work

### 6.1.1. Tapered multimode section to reduce the length

The length of the MMI devices can be minimized by carefully choosing the type of interference mechanism and by placing the access waveguides in allowed close proximity. Even though these two techniques are followed, as the number of channels increases, the device dimensions also increase. By tapering the multimode waveguide, the length of the device can be reduced [77]. This method will be very useful when the number of channels is higher. By tapering the multimode waveguide the length of the combiner can be made very suitable for integrated optics.

### 6.1.2. Pump/Signal combiner as an EDWA gain equalizer

The gain spectrum of an EDWA is not flat, rather peaked at 1530 nm resulting in a gain difference for different WDM channels. The multiplexer that was designed in this thesis can be used as a gain equalizer also. Instead of splitting the pump power equally, among all the signal channels, the pump channel should be split unequally [37]. Due to this, the pump power fed to different signal channels vary and hence the gain.

Designing this device will include optimization of a number of parameters, as they are required for the combiner designing. Additionally the power splitting also needs to be optimized. However, the same device can be used as a pump/signal combiner as well as a gain equalizer simultaneously. This reduces the cost and size of the amplifier module.

### 6.1.3. Improved light coupling methods

By changing the structure of the device access waveguides, the light coupling can be controlled such that it couples only to the waveguide. Instead of having the access waveguides on a single edge, they can be bent as shown in Figure 6.1. This ensures that the light coupled to the slab waveguide will not reach the multimode waveguide.

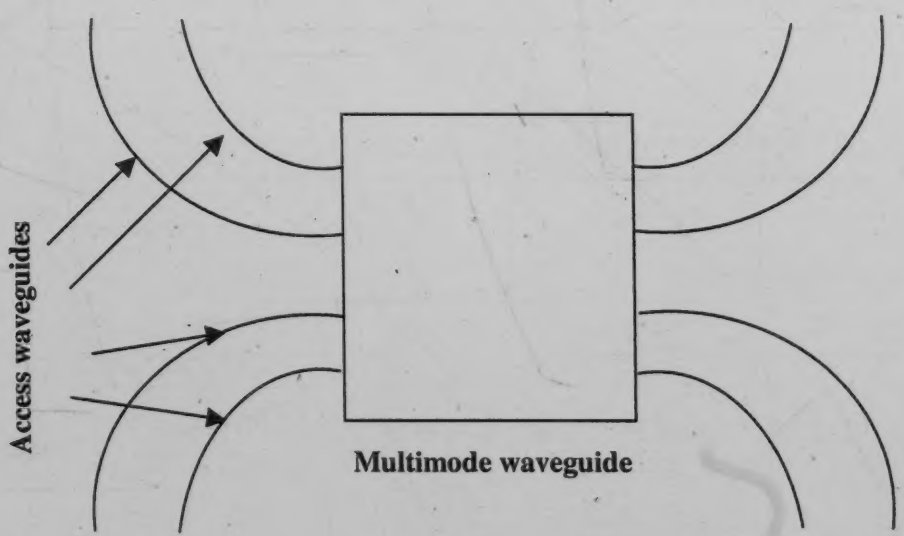


Figure 6.1 – Access waveguides for efficient coupling

Having the input fiber attached to a waveguide chip can also increase the ease of coupling. This chip should have a waveguide on it with the same dimensions as that of the access waveguides. The output of the chip waveguide is fed to the access waveguide. This ensures that the mode filed of the input light closely matches with that of the access waveguide and the power coupled to the slab waveguide will be reduced considerably. The potential difficulty in following this method is the alignment of fiber with the chip waveguide.

## References


[1] G. P. Agrawal, *Fiber-Optic Communication Systems*, Wiley Series in Microwave and Optical Engineering, 2002.

[2] S. V. Kartalopoulos, *Introduction to DWDM Technology*, IEEE Press, 2000.

[3] G. Keiser, *Optical Fiber Ccommunications*, McGraw-Hill series in Electrical Engineering, Communications and signal processing, 2000.

[4] N. Grote, H.Venghaus (Eds.) *Fiber Optic Communication Devices,* Springer-Verlag Berlin Heidelberg, 2001.

[5] R. N. Ghosh, J. Shmulovich, C. F. Kane, M. R. X. debarros, G. Nykolak, A. J. Bruce, and P.C. Becker, "8-mW threshold $Er^{3+}$-planar waveguide amplifier", *IEEE Photon. Tech. Lett.*, vol. 8, pp. 518-520, 1996.

[6] R. Shankar, *Erbium/Ytterbium Doped Planar Waveguide Amplifiers: Modeling and Fabrication*, MSc Thesis, University of Alberta, 2000.

[7] http://archive.mrv.com/products/infrastructure/products/oa/oa.php

[8] http://www.teemphotonics.com/

[9] http://sg.fujitsu.com/fqds/services/laser_01.html

[10] www.electrontubes.com

[11] M. P. Hehlen, M. J. Brinkman, S. R. Luthi, K. Nguyen, W. K. Bischel, "Multi-port EDFA for banded-channel amplification", in *OSA Trends in Optics and Photonics,* vol. 78, paper jw6, 2002.

[12] http://www.gemfirecorp.com/techMain.htm

[13] A. Tervonon, P. Poyhonen, S. Honkanen, and M. Tahkokorpi, "Analysis of symmetric directional coupler and asymmetric mach-zahnder interferometers as 1.30/1.55 μm dual wavelength demultiplexers/multiplexers", *Opt. Eng.*, vol. 32, pp. 2083-2091, 1993.

[14] R K. Sandberg and L. Leick "Novel design for integrated wavelength-flat 980/1550 nm pump-signal multiplexer" in *OSA Trends in Optics and Photonics,* vol. 78, paper ITH 13, 2002.

[15] F. Rottmann, A. Neyer, W. Mevencamp, and E. Voges. "Integrated-optic wavelength multiplexers on lithium niobate based on two-mode interference", J. *Lightwave. Technol.*, vol. 6, pp. 946-952, 1988.

[16] G.Zhang, S. Honkanen, A. Tervonen, C. M. Wu, and I. Najafi, "Glass integrated optics circuits for 1.48/1.55 and 1.33/1.55 μm wavelength division multiplexing and1/8 splitting", *Appl. Opt.*, vol. 33, pp. 3371-3374, 1994.

[17] T. Negami, H. Haga, and S. Yamamotto, "Guided-wave optical wavelength demultiplexer using an asymmetric Y junction", *Appl. Phys. Lett.*, vol. 54, pp. 1080-1082, 1989.

[18] M.R. Paiam, C. F. Janz, R. I. MacDonald, and J. N. Broughton, "Compact planar 980/1550 nm wavelength multi/ demultiplexer based on multimode interference", *IEEE Photon. Tech. Lett.*, vol. 7, pp. 1037-1039, 1995.

[19] M. Bachmann, M. K. Smit, P. A. Besse, E. Gini, H. Melchior, and L. B. Soldano, "Polarization-insensitive low-voltage optical waveguide switch using InGaAsP/InP four-port Mach-Zehnder interferometer", in *Optical Fiber Communications Conference and International Conference on Integrated Optics, OSA technical digest series,* vol. 4, 1993.

[20] L. B. Soldano, M. Bachmann, P. A. Besse, M. K. Smit, and H. Melchior, "Large optical bandwidth of InGaAsP/InP multimode interference 3-dB couplers", *Sixth European Conference on Integrated Optics*, Neuchatel, Switzerland, pp 18-22, 1993.

[21] A. Bhakhtazad, J. N. McMullin, C. J. Haugen, and R. G. Decorby, "MMI multiplexer for dual-channel erbium-doped waveguide amplifiers", *Opt. Exp.*, vol. 9, pp. 178-183, 2001.

[22] C. R. Pollock, *Fundamentals of Optoelectronics*, Richard D. Irwin, Inc, 1995.

[23] N. Ida, *Numerical Modeling for Electromagnetic Non-Destructive Evaluation,* T. J. Press, Chapman and Hall, UK, 1995.

[24] E. A. J. Marcatili, "Dielectric rectangular waveguide and directional coupler for integrated optics", *Bell Syst. Tech. J.*, vol. 48, pp. 2071-2102, 1969.

[25] P. C. Kendall, P. McIlroy, M. S. Stern, "Spectral index method for rib waveguide analysis", *Electron. Lett.*, vol. 25, pp. 107-108, 1989.

[26] G. B. Hocker and W. K. Burns, "Mode dispersion in diffused channel waveguides by the effective index method" *Appl. Opt.*, vol. 16, pp.113-118, 1977.

[27] K. S. Chiang "Performance of the effective-index method for the analysis of dielectric waveguides", *Opt. Lett.*, vol. 16, pp.714-716, 1991.

[28] V. Ramaswamy, "Strip loaded film waveguide", *Bell Syst. Tech. J.*, vol.53, pp. 697-705, 1974.

[29] R. A. Soref, J. Schmidtchen, and K. Petermann, "Large single-mode rib waveguides in GeSi-Si and Si-on-$SiO_2$", *IEEE. J. Quant. Elect.*, vol. 27, pp. 1971-1974, 1991.

[30] S. P. Pogossian, L. Vescan, and A. Vonsovici, "The single-mode condition for semiconductor rib waveguides with large cross section", *J. Lightwave. Technol.*, vol. 16, pp. 1851-1853, 1998.

[31] E. A. J. Marcatili, "Slab coupled waveguides", *Bell Syst. Tech. J.*, vol. 53, pp. 645-674, 1974.

[32] O. Bringdahl, "Image formation using self-imaging techniques", *J. Opt. Soc. America*, vol. 63, pp. 416-419, 1973.

[33] R. Ulrich, "Image formation by phase coincidences in optical waveguides", *Opt. Commun.*, vol. 13, pp. 259-264, 1975.

[34] L. B. Soldano and E. C. M. Pennings, "Optical multi-mode interference devices based on self-imaging: principles and applications", *J. Lightwave Technol.*, vol. 13, pp. 615-627, 1995.

[35] N. S. Kapany and J. J. Burke, *Optical Waveguides*, New York: Academic, 1972.

[36] M. Bachmann, P. A. Besse, and H. Melchior, "General self –imaging properties in NxN multimode interference couplers including phase relations", *Appl. Opt.*, vol. 33, pp. 3905-3911, 1994.

[37] M. Bachmann, P. A. Besse, and H. Melchior, "Overlapping-image multimode interference couplers with a reduced number of self-images for uniform and non uniform power splitting", *Appl. Opt.*, vol. 34, pp. 6898-6910, 1995.

[38] R. Scarmozzino, A. Gopinath, R. Pregla, and S. Helfert, "Numerical techniques for modeling guided-wave photonic devices", *IEEE J. Select. Topics Quantum Electron.*, vol. 6, pp. 150-162, 2000.

[39] H. J. W. M. Hoekstra, G. J. M. Krijinen, and P. V. Lambeck, "New formulations of the beam propagation method based on the slowly varying envelope approximation", *Opt. Commun.*, vol. 97, pp. 301-303, 1993.

[40] http://www.c2v.biz/software/olympios/demos.shtml

[41] G. R. Hadley, "Wide-angle beam propagation using Pade approximant operators", *Opt. Lett.*, vol. 17, pp. 1426, 1992.

[42] I. Ilic, R. Scarmozzino, and R. M. Osgood Jr., "Investigation of the Pade approximant – based wide-angle beam propagation method for accurate modeling of waveguide circuits", *J. Lightwave Technol.*, vol. 14, pp. 2813-2822, 1996.

[43] R. Decorby, *Course notes for EE 682*, University of Alberta, 2002.

[44] E. C. M. Pennings, R. van Roijen, M. J. N van Stralen, P. J. de Waard, R. G. M. P. Koumans and B. H. Verbeek, "Reflection properties of multimode interference devices", *IEEE Photon. Tech. Lett.*, vol. 6, pp. 715-718, 1994.

[45] L. Elada, "Advances in Telecom and Datacom Optical Components", *Opt. Eng.*, vol. 40, pp. 1165-1178, 2001.

[46] T. Kitagawa, K. Hattori, Y. Hibino, and Y. Ohmori, "Neodymium doped silica-based planar waveguide lasers", *J. Lightwave Technol.*, vol. 12, pp. 436-442, 1994.

[47] T. Kitagawa, K. Hattori, K. Shuto, M. Yasu, M. Kobayashi, and M. Horigushi, "Amplification in erbium–doped silica –based planar lightwave circuits", *Electron. Lett.*, vol. 28, pp. 1818-1819, 1992.

[48] Q. Lai, M. Bachmann, and H. Melchior, "Low-loss 1xn mulitmode interference couplers with homogeneous output power distributions realized in silica on si material", *Electron. Lett.*, vol. 33, pp. 1699-, 1997.

[49] C. R. Doerr, "Cascaded Planar Waveguide Arrays," *OSA TOPS WDM Components,* vol. 29, 1999.

[50] T. Goh, M. Yasu, K. Hattori, A. Himeno, M. Okuno, and Y. Ohmori, "Low-loss high extinction ratio silica based strictly non-blocking 16x16 thermo-optic matrix switch", *IEEE Photon. Tech. Lett.*, vol. 10, pp. 810-812, 1998.

[51] M. Lenzi, S. Tebaldini, D. Di Mola, S. Brunazzi, and L. Cibinetto, "Power control in the photonic domain based on integrated arrays of optical variable attenuators in glass-on-silicon technology", *IEEE J. Select. Topics Quantum Electron.*, vol. 5, pp. 1289-1297, 1999.

[52] U. Fischer, T. Zinke, J. R. Kropp, F. Arndt, and K. Petermann, "0.1 dB/cm waveguide losses in single-mode SOI rib waveguides", *IEEE Photon. Tech. Lett.*, vol. 8, pp. 647-648, 1996.

[53] K. Worhoff, P. V. Lambeck, and A. Driessen, "Design, tolerance analysis, and fabrication of silcion oxynitride based planar optical waveguides for communication devices", *J. Lightwave Technol.*, vol. 17, pp. 1401-1407, 1999.

[54] R. M. de Ridder, K. Worhoff, A. Driessen, P. V. Lambeck and H. Albers, "Silicon oxynitride planar waveguiding structures for application in optical communication", *IEEE J. Select. Topics Quantum Electron.*, vol. 4, pp. 930-937, 1998.

[55] R. M. de Ridder, A. F. M. Sander, A. Driessen, and J. H. J. Fluitman, "An integrated optic adiabatic TE/TM mode splitter on silicon", *J. Lightwave Technol.*, vol. 11, pp. 1806-1811, 1993.

[56] B. J. Offrein, R. Germann, F. Horst, H. W. M. Salemink, R. Beyeler, and G. L. Bona, "Resonant coupler-based tunable add-after-drop filter in silicon-oxynitride technology for WDM networks", *IEEE J. Select. Topics Quantum Electron.*, vol. 5, pp.1400-1406, 1999.

[57] B. J. Offrein, R. Germann, F. Horst, H. W. M. Salemink, R. Beyeler, and G. L. Bona, "Adaptive gain equalizer in high index contrast SiON technology", *IEEE Photon. Tech. Lett.*, vol. 12, pp.504-506, 2000.

[58] L. Peters, "SOI Takes over Where Silicon Leaves off", *Semiconductor International*, vol. 16, pp. 48-51, 1993.

[59] P. D. Trinh, S. Yegnanarayanan, F. Coppinger and B. Jalali, "Compact multi-mode interference couplers in silicon-on-insulator technology," in *Conf. Lasers and Electro-Optics*, CLEO'97, Baltimore, MD, paper cThV4, 1997.

[60] P. D. Trinh, S. Yegnanarayanan, and B. Jalali, "Integrated optical directional couplers in silicon-on –insulator", *Electron. Lett.*, vol. 31, pp. 2097-2098, 1995.

[61] P. D. Trinh, S. Yegnanarayanan, and B. Jalali, "5x9 Integrated Optical Star Coupler in Silicon-on Insulator Technology", *IEEE Photon. Tech. Lett.*, vol. 8, pp. 794-796, 1996.

[62] P. D. Trinh, S. Yegnanarayanan, F. Coppinger, and B. Jalali, "Silicon-on-insulator (SOI) phased-array wavelength multi-demultiplexer with extremely low-polarization sensitivity", *IEEE Photon. Tech. Lett* ., vol. 9, pp. 940-942, 1997.

[63] A. V. P. Kesan, P. G. May, E. Bassous, and S. S. Iyer, "Integrated waveguide-photodetector using Si/SiGe multiple quatntum wells for long wavelength applications," in Proc. IEDM, San Fransisco, CA 1990, pp. 285-588, 1990.

[64] T. Yoshimoto, S. Thomas, K. L. Wang, and B. Jalali, "Waveguide-fed SiGe avalanche pin photodetector grown on SOI substrate with 0.2A/W external responsivity at 1.3 μm," in Tech. Dig. Integrated Photonic Research (IPR'98), Victoria, BC, Canada, pp. 285-288, 1998.

[65] B. Jalali, S. Yegnanarayanan, T. Yoon, T. Yoshimoto, I. Rendina, and F. Coppinger, "Advances in silicon-on-insulator optoelectronics", *IEEE J. Select. Topics. Quantum. Electron.*, vol. 4, pp. 938-947, 1998.

[66] http://www.c2v.nl/software/olympios/modules/tempselene.shtml

[67] P. A. Besse, Maurus Bachmann, H. Melchior, L. B. Soldano, and M. K. Smit, "Optical bandwidth and fabrication tolerances of multimode interference couplers", *J. Lightwave Technol.*, vol. 12, pp. 1004-1009, 1994.

[68] Marc J. Madou, *Fundamnetals of Microfabrication*, CRC Press 2002.

[69] http://www.adtekphotomask.com/

[70] M. Brett, *Course notes for EE 642*, University of Alberta, 2001.

[71] D. B. Lee, "Anisotropic etching of Silicon", *J. Appl. Phys.*, vol. 40, pp. 4569-74, 1969.

[72] J. Bhardwaj, H. Ashraf, A. McQuarrie, "Dry silicon etching for MEMS", *J. Elec. Chem. Soc., The symposium on microstructures and microfabricated systems*, 1997.

[73] J. Bhardwaj, H. Ashraf "Advanced silicon etching using high density plasmas", Proc. SPIE, Micromachining and Microfabrication process technology, pp. 224-233, 1995.

[74] K. R. Williams, Richard S. Muller, "Etch rates for Micromachining processing", *IEEE J. Microelectromechanical Sys.*, vol. 5, pp. 256-269, 1996.

[75] V. R. Subramanian, *Fabrication of bragg gratings in silicon-on-insulator technology*, MSc Thesis, University of Alberta, 2002.

[76] H. Nishihara, M. Haruna, Toshiaki Suhara, *Optical integrated circuits*, McGraw-Hill optical and electro-optical engineering series, 1989.

[77] D. S. Levy, R. Scarmozzino and Richard M. Osgood, Jr, "Length reduction of tapered NxN MMI devcies", *IEEE Photon.Tech. Lett.*, vol. 10, pp. 830-832, 1998.